remote sensing

MDPI

Article

Generating High-Quality and High-Resolution Seamless Satellite Imagery for Large-Scale Urban Regions

Xinghua Li [1,†], Zhiwei Li [2,†], Ruitao Feng [2], Shuang Luo [2], Chi Zhang [2], Menghui Jiang [2] and Huanfeng Shen [2,3,4,*]

1 School of Remote Sensing and Information Engineering, Wuhan University, Wuhan 430079, China; lixinghua5540@whu.edu.cn
2 School of Resource and Environmental Sciences, Wuhan University, Wuhan 430079, China; lizw@whu.edu.cn (Z.L.); ruitaofeng@whu.edu.cn (R.F.); sluo@whu.edu.cn (S.L.); whuzhangchi95@whu.edu.cn (C.Z.); jiangmenghui@whu.edu.cn (M.J.)
3 Collaborative Innovation Center of Geospatial Technology, Wuhan 430079, China
4 Key Laboratory of Geographic Information System, Ministry of Education, Wuhan University, Wuhan 430079, China
* Correspondence:shenhf@whu.edu.cn; Tel.: +86-27-6877-8375
† These authors contributed equally to this study and shared the first authorship.

Received: 9 November 2019; Accepted: 20 December 2019; Published: 24 December 2019

Abstract: Urban geographical maps are important to urban planning, urban construction, land-use studies, disaster control and relief, touring and sightseeing, and so on. Satellite remote sensing images are the most important data source for urban geographical maps. However, for optical satellite remote sensing images with high spatial resolution, certain inevitable factors, including cloud, haze, and cloud shadow, severely degrade the image quality. Moreover, the geometrical and radiometric differences amongst multiple high-spatial-resolution images are difficult to eliminate. In this study, we propose a robust and efficient procedure for generating high-resolution and high-quality seamless satellite imagery for large-scale urban regions. This procedure consists of image registration, cloud detection, thin/thick cloud removal, pansharpening, and mosaicking processes. Methodologically, a spatially adaptive method considering the variation of atmospheric scattering, and a stepwise replacement method based on local moment matching are proposed for removing thin and thick clouds, respectively. The effectiveness is demonstrated by a successful case of generating a 0.91-m-resolution image of the main city zone in Nanning, Guangxi Zhuang Autonomous Region, China, using images obtained from the Chinese Beijing-2 and Gaofen-2 high-resolution satellites.

Keywords: cloud detection and removal; high-quality and high-resolution; mosaicking; pansharpening; remote sensing

1. Introduction

The generation of a high-quality seamless urban geographical map is significant for urban land-use mapping and urban land planning [1–4]. Generally, high-spatial-resolution images (HRIs) from satellite remote sensing platforms are required for precise urban mapping. In recent years, small satellites, as a new generation of satellites, have received extensive attention and developed rapidly because of their light weight, small volume, low cost, and flexible launch capability. In addition, small satellites can be further netted as distributed constellations which facilitate the acquisition of high-spatial-resolution remote sensing images with a high imaging quality and short revisit cycle. However, several issues must be considered during urban image generation with small satellite HRIs,

such as Beijing-2, as shown in Figure 1. HRIs can be divided into the issues coming from an individual image and the issues arising amongst multiple images.

On the one hand, a single optical satellite image will inevitably be affected by a high proportion of haze and cloud cover [5–7]. Thus, dehazing and cloud removal should be utilized to obtain a clear and spatially seamless image. These issues come from individual images that make generating a high-quality seamless urban image a challenging task. On the other hand, for imagery containing multispectral and panchromatic bands, the spatial resolution of the multispectral image and the spectral resolution of the panchromatic image can be enhanced by fusing them. Thus, pansharpening [8–10] is also required. Furthermore, the swath width of images is usually reduced with an increase in spatial resolution. Thus, image mosaicking is an essential step for large-scale urban image generation [11–13] but is accompanied by new problems. Geometric misalignment and radiometric incoherency in adjacent images can cause seam lines in the image mosaicking process. Hence, image registration and radiometric normalization must be conducted [14–16], which also brings new challenges to the procedure of urban image generation.

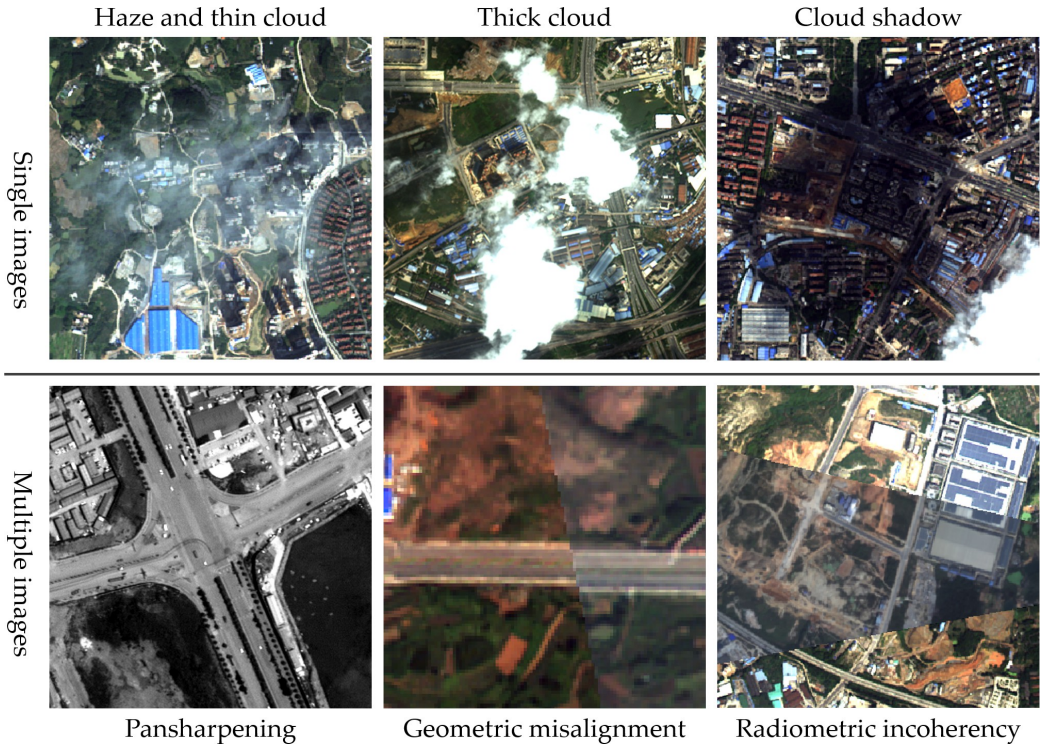

Figure 1. Issues to be addressed for generating high-quality seamless images.

These issues are currently tackled independently and inefficiently. Thus, suitable images are often unavailable to be merged into an urban image. The lack of a systematic solution and the requirements of urban mapping are the motivations for developing an integrated procedure to address the abovementioned issues. In this study, a procedure for high-quality seamless urban image generation, integrating image registration, dehazing and thin cloud removal, thick cloud detection and removal, pansharpening, and image mosaicking is proposed. Specifically, our attention is focused on cloud removal, including a novel spatially adaptive method for removing thin clouds with non-uniform atmospheric light and a stepwise local moment matching (SLMM) method for removing thick clouds. The case study of the main city zone of Nanning, Guangxi Zhuang Autonomous Region, China, shows the generated results of the procedure. The experimental results confirm that the proposed procedure is a promising and effective way for generating large-scale high-quality seamless images of urban areas.

The remainder of this paper is organized as follows. Section 2 discusses the related works. Section 3 describes the proposed procedure and method for generating a high-quality seamless urban

image from satellite HRIs. Section 4 explains the experimental results, and Section 5 provides a discussion. Section 6 presents the conclusion.

2. Related Works

Haze/thin cloud frequently appears in optical remote sensing images, resulting in reduced image contrast and blurred surface color [17]. In general, existing thin cloud removal methods can be divided into two categories: (1) radiative transfer model (RTM)- and (2) statistical information (SI)-based methods. The RTM-based methods simulate the imaging process to correct the clouds by introducing atmosphere-, surface- and sensor-related parameters [18,19]. This type of method is rigorous in theory but requires numerous parameters. The RTM-based methods are unsuitable for use with high-resolution remote sensing images because the local horizontal difference of the atmosphere is insufficiently considered. SI-based methods mine the statistical characteristics of clouds in the spatial and spectral domains to correct the imagery. Typical methods include filtering in the frequency domain [17,20], dark channel prior (DCP)-based methods [21–24], and spectral transformation-based methods [25–28]. These methods can remove clouds without any prior knowledge and can be combined with an RTM method to achieve an accurate correction [29]. However, statistical characteristics are not always suitable for the complex scenes acquired from different sensors. Furthermore, the influences of uneven scattering in the spatial domain are usually ignored, resulting in uneven haze not being completely removed. For high-resolution remote sensing images with complex scenes and uneven haze, the development of a general thin cloud removal method is urgently required.

Thick clouds and the accompanying shadows are inevitable contaminants for optical imagery in the range of visible and infrared spectra. Such contaminants lead to information loss and influence the availability of satellite data. In recent years, scholars have undertaken many studies of cloud detection and removal. Most of the current cloud detection methods screen the clouds in images by rule-based classification, which is based on the discriminative spectral features of the cloud and shadow [30–32]. However, cloud detection in high-resolution images is more difficult than in medium-resolution images due to the insufficient spectral information. Thus, additional spatial features, such as geometric and texture features, have been combined with spectral features to obtain improved cloud detection results [33,34]. In addition, deep learning has been introduced in cloud detection and has obtained satisfactory results, benefiting from the advantage of adaptively learning discriminative features [35]. Cloud removal for cloud-contaminated imagery follows after a cloud and shadow mask have been acquired; it is essentially an information reconstruction process [7], which usually relies on temporal complementary information from one or more cloud-free images of adjacent dates [36–38]. The temporal-based cloud removal methods have been intensively studied and are a promising way for handling thick clouds [39–41]. However, the spectral and spatial details of the cloud-removed region should be further enhanced for remote sensing HRIs.

Pansharpening is conducted for the spatial resolution improvement of multispectral images. Numerous pansharpening algorithms have been developed in recent decades, which can generally be divided into four main categories: (1) component substitution (CS)- [42–44], (2) multiresolution analysis (MRA)- [45–47], (3) variational optimization (VO)- [48–50] and (4) deep learning (DL)-based methods [9,51,52]. Amongst these methods, the CS- and MRA-based methods are the fastest and the most commonly used. Most professional remote sensing software packages, such as ENVI and ERDAS Imagine, provide pansharpening algorithms belonging to the CS-based category. The VO-based methods were developed after the first two categories and are based on a solid mathematical foundation. The DL-based methods fully utilize the powerful learning capability of neural networks and are currently the state-of-the-art algorithms in pansharpening.

The main urban areas often cannot be covered in only one image due to the limitations of the imaging swath width or imaging mechanism. Stitching or mosaicking multiple images from different periods or sensors is often a necessary order to capture the full target area [14,53–55]. Image registration [56] is usually required before the mosaicking of multiple images. The existing image registration algorithms can be classified into two categories, namely, area- and feature-based

methods. The area-based methods fully utilize the intensity information, and the emphasis is placed on the similarity metric construction, such as correlation coefficients (CC), mutual information (MI) [57], and normalized correlation coefficients (NCC) [58]. Feature-based methods use distinct features, such as points, lines, and regions, to represent the image to be registered. The most representative feature extraction algorithms, such as scale-invariant feature transform (SIFT) [59] and speeded-up robust features (SURF) [60], are mostly utilized in feature-based frameworks. In addition, many excellent algorithms for image mosaicking exist, which generally consists of radiometric normalization [61–65], seam line detection [66–68] and image blending [14,69–71]. However, image registration, radiometric normalization, and seam line detection are still challenging tasks for the mosaicking of high-resolution remote sensing images.

Image registration, radiometric calibration, and image blending are fundamental steps for addressing the issues of geometric misalignment, radiometric incoherency, and large-scale maps, respectively. The objective is to generate a large-scale image that involves multiple scenes. However, the mosaicking of HRIs is more difficult than that of lower-resolution images. Achieving accurate image registration, which is essential for image mosaicking, is difficult due to the limited imaging angle and land-cover changes. The determination of the seam lines for the images to be mosaicked is also important for seamless mosaicking and is often a time-consuming process. Furthermore, the other issues shown in Figure 1, including haze and thin cloud, thick cloud, cloud shadow, and pansharpening, are not all covered in the existing literature. Most of the studies have addressed these issues separately. For example, cloud cover is usually considered when mosaicking remote sensing images. On the one hand, clouds are often handled independently by scholars in terms of cloud detection and removal. Roy et al. [72] utilized cloud masking to generate mosaics of the conterminous United States. The generation of sea ice maps is further dependent upon cloud removal in the compositing process [73,74]. On the other hand, certain other issues have also been addressed, in addition to clouds. Helmer and Ruefenacht [12] used regression tree prediction and histogram matching for seamless mosaicking to support change detection in persistently cloudy regions of Landsat images. Hewson et al. [75] reduced the effects of atmospheric and surface scattering through atmospheric water vapor correction and cloud/shadow masking for the seamless geological map generation of the Broken Hill–Curnamona province of Australia, using ASTER imagery. Zhang et al. [76] considered cloud cover and geometric correction in the workflow to produce digital orthophoto maps over a national scale. Li et al. [77] applied cloud masking and image pansharpening techniques to produce a cloud shadow-free and high-resolution mosaic based on co-registered IKONOS images. In addition, attention has been paid to the radiometric differences. Du et al. [78] combined radiometric normalization with pixel-wise compositing and quality control in the process of mosaicking high-resolution satellite images. Radiometric balancing has also been applied in the image mosaic generation of ASTER thermal infrared data [79]. In summary, a comprehensive and effective procedure is required to generate a high-quality seamless and large-scale urban image from high-spatial-resolution satellite images.

3. Method

In this study, a procedure is proposed for high-quality seamless urban image generation from high-resolution satellite images. Methodologically, a spatially adaptive method considering the uneven atmospheric scattering and a novel algorithm known as SLMM are correspondingly proposed to remove the thin and thick clouds of the images, respectively. Figure 2 shows the framework of the proposed procedure. The images are initially pre-processed by systematic geometric correction and then classified into target and auxiliary images. The target images are determined as images that are close to the target date and have good quality, whereas the auxiliary images are selected on the basis of the cloud cover of the target images. The step of dehazing and thin cloud removal is then conducted for the target images covered by haze and thin clouds. Subsequently, the cloud-contaminated target images are transferred for thick cloud removal on the basis of the results of thick cloud detection. The cloud-free multispectral and panchromatic images are combined for pansharpening and mosaicking after overlapping image registration. Finally, the

high-quality seamless urban image of the target area can be obtained by the post-processing steps, including target area clipping and radiometric adjustment.

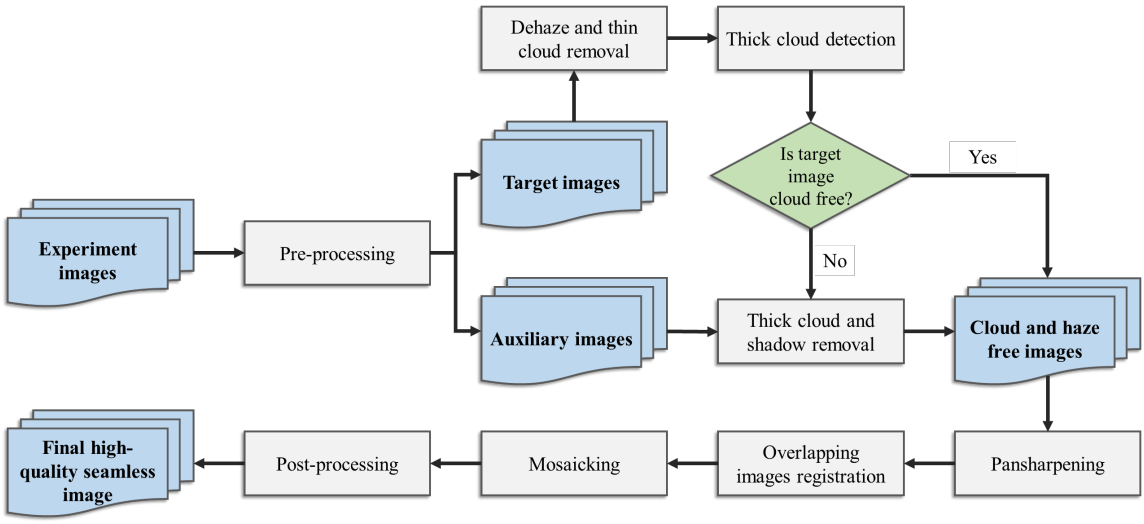

Figure 2. Framework of the procedure for high-quality seamless image generation.

3.1. Pre-Processing

In the pre-processing steps, all available remote sensing images are initially resampled to the same resolutions for multispectral and panchromatic images after systematic geometric correction. Subsequently, all images are classified into target and auxiliary images. The target images are close to the target date (e.g., yearly/seasonally/monthly period depending on available images and users' purposes after considering possible land cover changes due to vegetation phenology and urban expansion, etc.) and have a good quality in the target area, whereas the auxiliary images are selected on the basis of the cloud cover of the target images. The cloud cover percentages can be derived from the image header files or estimated by the existing cloud detection methods. However, considering the low accuracy of the provided cloud cover percentages or masks, a more accurate cloud detection method should thus be utilized. Finally, image registration is applied to eliminate possible misalignments between the multispectral and panchromatic images, and cloudy regions in the target and reference images, respectively. The area-based method has a weak capability to handle large geometrical deformation and is time-consuming. Thus, a feature-based method is adopted to register the images, implemented by the steps shown in Figure 3, in which sensed images denote the images to be registered.

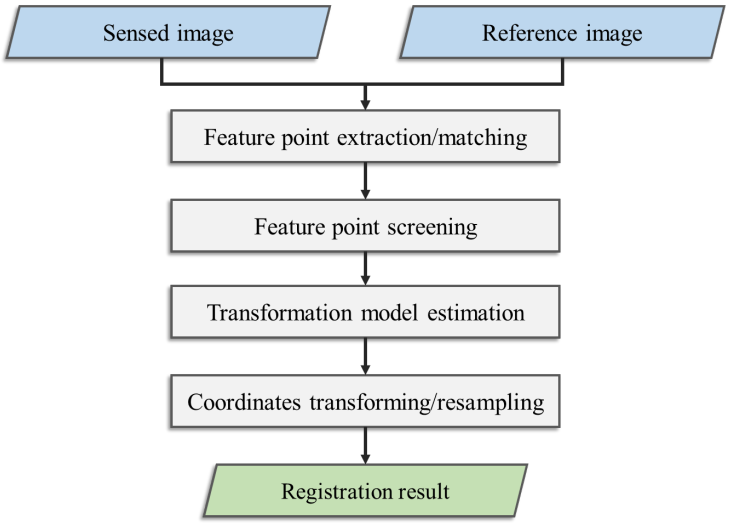

Figure 3. Image registration process.

Following the image registration process, the reference and sensed images are input into ENVI. Most of the distinct feature points are extracted and matched with the corresponding points in the sensed image via the template matching algorithm. However, considering that the ranges of the images to be registered are large, and that a global transformation model will be estimated, the extracted feature points should be distributed uniformly and sparsely. Such feature points can be achieved by combining necessary manual adjustments. The feature points are empirically extracted in the building corners, road intersections and so on to supplement the feature points locally. With the satisfactory feature points, the geometrical relationship between the reference and sensed images is calculated by a linear polynomial model. The coordinates in the sensed image are then transformed and resampled by a bilinear interpolation algorithm. The same process is also used to register the corresponding target and auxiliary images and the corresponding panchromatic and multispectral images to alleviate the geometrical displacement.

3.2. Dehazing and Thin Cloud Removal

In this study, a spatially adaptive haze removal method is proposed on the basis of the DCP [21] and hazy image model [80–82]. The variation of atmospheric scattering, which is effective in removing uneven haze and producing a vivid result, is considered. The DCP is a statistical law that states that the intensity of certain pixels in local patches tends to be zero in at least one or several channels for the non-sky regions of clear images. The hazy image model describes the radiance composition of images under a turbid atmosphere, which can be expressed as [21]

$$I(x) = J(x)t(x) + A(1 - t(x)) \quad (1)$$

where I is the hazy/thin cloud image, J denotes the clear image, t is the transmission, and A is the atmospheric light. Thus, we can remove the haze/thin cloud via the hazy image model if A and t are available. Figure 4 depicts the flowchart of the haze/thin cloud removal procedure.

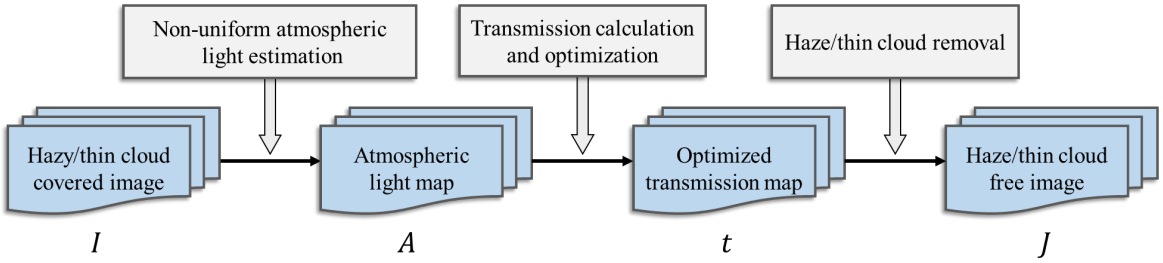

Figure 4. Flowchart of haze/thin cloud removal.

In theory, the portion of the path radiance that is scattered and reaches the sensor will correspond to atmospheric light A in the hazy image model. However, the atmospheric light is usually assumed to be a constant in the entire scene. This assumption is true for an image covered with uniform haze, such as most natural images. The reason is that the scattering intensities of these images are relatively stable, and the scattered path radiance reaching the sensor will be almost the same in the entire scene. However, remote sensing images have particularly broad imaging range and are often covered with uneven haze. For such images, the scattered path radiance will vary in the spatial dimension, suggesting that the atmospheric light should be spatially varied. Therefore, developing an estimation algorithm that reflects the spatial characteristic of atmospheric light is necessary.

Changes in scattering intensity generally cause uneven luminance in the image, indicating that the luminance can reflect the scattering intensity distribution in space. Therefore, the luminance is an important clue for estimating non-uniform atmospheric light. On the basis of the above analysis, we propose a luminance-based atmospheric light estimation strategy, entitles the non-uniform atmospheric light model. This model can be defined as follows:

$$A_{nua} = A_{basic} + \Delta A_{local} \quad (2)$$

where A_{nua} is the non-uniform atmospheric light and A_{basic} and ΔA_{local} are the basic atmospheric light and atmospheric light increment, respectively. The former is a constant and the latter is a variable related to the haze heterogeneity.

The non-uniform atmospheric light of an arbitrary image is given by the following two steps: (1) calculating the atmospheric light increment from the luminance fieldw and (2) estimating the basic atmospheric light from the original image. Firstly, a Gaussian low-pass filter is selected to obtain the luminance from the hazy image. As the atmospheric light is locally stable, a minimum filter is adopted to post-process the luminance. Hence, the increment can be expressed as

$$\Delta A_{local} = \min_{\Psi} \tilde{I} + \tilde{I}_{min} \quad (3)$$

where $\tilde{I}$ is the luminance of the image, $\min_{\Psi} \tilde{I}$ is a minimum filter with window Ψ, in which the window size is related to the heterogeneity of the haze, $\tilde{I}_{min}$ is the minimum of $\tilde{I}$, and ΔA_{local} is the estimated atmospheric light increment.

To calculate the basic atmospheric light A_{basic}, the 0.1% pixels with the largest dark channel intensity, which are calculated by the traditional DCP, are initially selected. Moreover, one of the pixels with the largest intensity is regarded as the value of basic atmospheric light. Once A_{basic} and ΔA_{local} are obtained, the non-uniform atmospheric light of the input image can be estimated via Equation (2). With A, the transmission of the image can be calculated and the haze/thin cloud-free image can finally be acquired. In addition, for the panchromatic channel, A and t are upsampled to the same size to remove haze/thin cloud.

3.3. Thick Cloud Detection and Removal

For the thick cloud of the high-resolution images, a cloud detection method and a cloud removal method are introduced in the following content.

3.3.1. Thick Cloud Detection

The multi-feature combined (MFC) method proposed by Li et al. [33] is used to screen cloud and cloud shadow in the haze/thin cloud-free images on the basis of the results of the dehazing and thin cloud removal. Figure 5a shows the process flow of the MFC algorithm. The MFC method combines multiple features (i.e., spectral, shape and texture) to implement object-based cloud and shadow detection. MFC initializes a rough cloud mask on the basis of spectral threshold segmentation, and the core cloud regions are captured after this step. A fine mask is then produced by applying guided filtering and binarization processing, in which the thin clouds around the cloud boundaries are captured. Finally, the non-cloud bright objects in the refined cloud mask are removed by using object-based shape and texture features to improve the cloud detection results and produce the final cloud mask. Furthermore, a cloud shadow mask is obtained on the basis of the cloud mask, which is screened by associating clouds and the detected shadows through object-based matching and correction, with the aid of satellite viewing and solar angles. Notably, a higher priority is set for cloud than cloud shadow in the final mask.

The MFC method was originally proposed for Gaofen-1 wide-field-of-view imagery, which contains three visible bands and a near-infrared band. It can also be applied to other types of imagery that have similar band settings. In this study, MFC is used to produce cloud and cloud shadow masks for the experimental images after parameter optimization. Several key spectral thresholds in MFC are manually fine-tuned through a series of tests and parameter-sensitive analyses. Manual correction is required in a few cases because cloud and cloud shadow detection for high-resolution images is challenging, and the results produced by MFC are not completely accurate. Subsequently, the corrected masks are used as guidance for the subsequent cloud and cloud shadow removal.

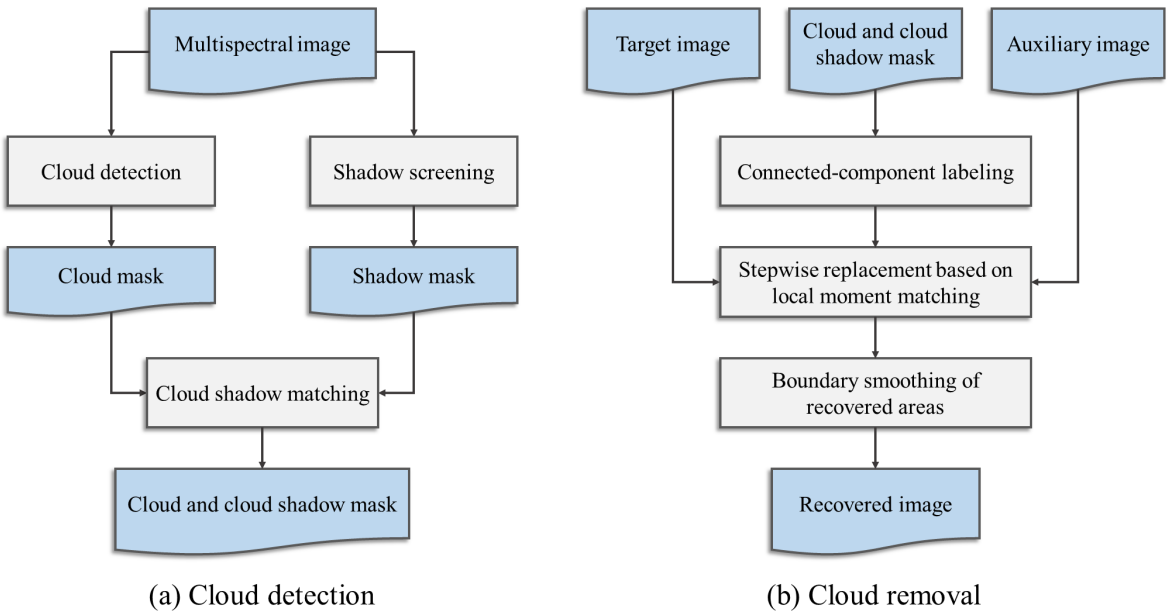

Figure 5. Flowcharts of the cloud detection method and proposed cloud removal method. (**a**) Flowchart of cloud detection. (**b**) Flowchart of cloud removal.

3.3.2. Thick Cloud Removal

In this study, a simple but effective cloud removal method based on SLMM is proposed to recover the cloud-contaminated areas. The proposed SLMM cloud removal method has fidelity advantages for the spectral and spatial details in the recovered cloud-contaminated regions. Figure 5b illustrates the flowchart of the SLMM method. The inputs of the method are the target image that should be recovered, the cloud and cloud shadow mask of the target image, and the auxiliary image, which is another temporal image covering the same area as the target image. Assuming that the auxiliary image is cloud-free and has been registered with the target image, our goal is to recover the cloud-contaminated areas in the target image by combining the complementary information from the auxiliary image whilst ensuring that the recovered areas are seamless.

The proposed SLMM method consists of three main steps. Initially, connected component labeling is conducted, in which the pixels marked as cloud or cloud shadow in the target mask and connected in eight neighbours are labeled as independent objects. Then, as shown in Figure 6, each target image patch T located around an object can be acquired by extending the height and width of the object's bounding rectangle (black rectangle in Figure 6a) with specific pixels (e.g., 200) in all four sides. For each patch T, the SLMM procedure is implemented to recover the contaminated areas pixel by pixel through stepwise replacement. Notably, the contaminated areas to be recovered are labeled in the target mask and recovered along the cloud object boundaries to the center. Such a process can be controlled by stepwise one-pixel erosion of the target mask, in which recovered pixels are treated as the known cloud-free pixels and involved in the recovery of the remaining contaminated pixels labeled in the target mask. Specifically, the recovered cloud-contaminated pixel $T(i,j)$ at (i,j) in the target image patch can be acquired by the linear transformation of pixel $R(i,j)$ in the auxiliary image, as shown in Equation (4). Such pixel involves valid and cloud-free pixels in local window k centred at (i,j) in the target and auxiliary image patches. The linear transformation in Equation (4) is also called local moment matching, where σ_T and σ_R are the standard deviation of the valid pixels in k in the target and auxiliary image patches, respectively. Moreover, μ_T and μ_R are the corresponding mean values. Notably, the size of window k is equal to $2r + 1$, where r is empirically set to 80 in the experiments of this study. Finally, boundary smoothing is conducted at one-pixel outer and inner edges of the recovered areas to eliminate edge effects. Consequently, the Gaussian smoothing kernel is empirically set with a size of 3 × 3 and a standard deviation of 1.6. The contaminated areas in the target image are recovered object by object and channel by channel.

$$T(i,j) = \frac{\sigma_T}{\sigma_R} \cdot R(i,j) + \mu_T - \frac{\sigma_T}{\sigma_R} \cdot \mu_R \quad (4)$$

The stepwise strategy progressively recovers the contaminated pixels from object boundaries to the center and treats the recovered pixels as cloud-free pixels. In addition, this strategy makes the proposed cloud removal method effective for large-scale thick cloud removal, specifically in high-resolution images. The spatial details from the auxiliary image can be well preserved in the recovered areas because the SLMM method is a type of intensity adjustment-based method.

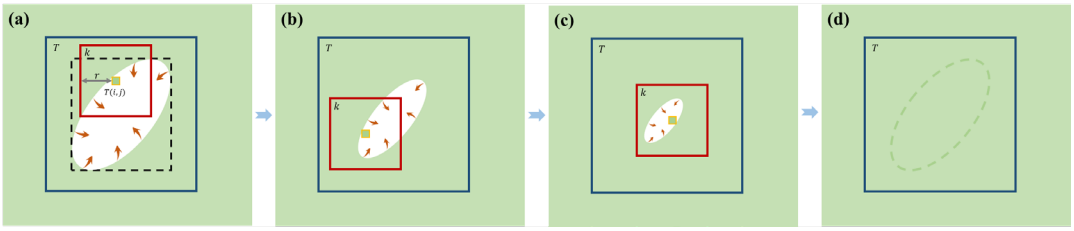

Figure 6. Illustration of the stepwise recovery of a cloud-contaminated area using SLMM. (**a**) Target image to be recovered. (**b**,**c**) Target image partly recovered through stepwise replacement, in which the recovered pixels in (**b**) are treated as cloud-free pixels and involved in the recovery of the remaining contaminated pixels in (**c**). (**d**) Recovered target image.

3.4. Pansharpening

The fast pansharpening algorithm used in this study is based on the CS-based fusion framework and fully utilizes the high efficiency of the CS-based method [10,83]. Figure 7 depicts the flowchart of the proposed pansharpening method, which can be represented as:

$$MS_k = \widetilde{MS_k} + \beta_k(P - I) \quad (5)$$

where $k = 1,\cdots,N$, MS is the fused high-spatial-resolution multispectral (HR-MS) image and $\widetilde{MS}$ is the low spatial resolution multispectral (LR-MS) image upsampled to the scale of the panchromatic (PAN) image. N is the band number of the multispectral image, and the subscript k indicates the kth spectral band. I is the intensity component of $\widetilde{MS}$, which is calculated by a linear combination of spectral bands in $\widetilde{MS}$, where the linear combination coefficient w_k is obtained by Equation (6). P represents the PAN image. The histogram match is performed between P and I to make P and I have the same mean and variance values, which can reduce the spectral distortion [83] caused by the gap between the two data levels. β is the band-dependent injection weight, which is calculated by the average gradient of each spectral band in the LR-MS image, as shown in Equation (7).

$$P_l = \sum_{k=1}^{N} w_k MS_k, \quad (6)$$

where P_l is the PAN image downsampled to the size of the LR-MS image, that is, MS_k in Equation (6). The linear combination coefficient w_k is obtained on the basis of least square fitting.

$$\beta_k = \frac{gra(\widetilde{MS_k})}{gra(I)} \quad (7)$$

where $gra(\cdot)$ is the function for obtaining the average gradient of the image. The average gradient is the mean value of the gradients of all pixels in the image.

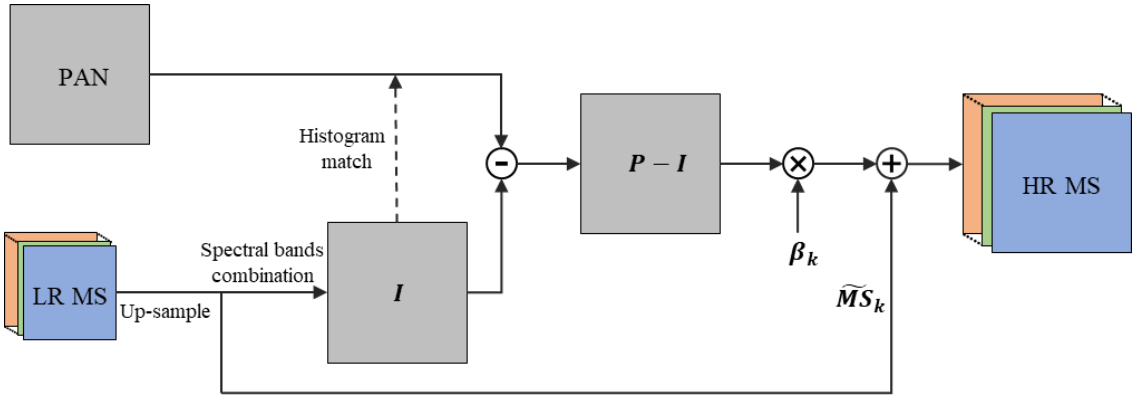

Figure 7. Flowchart of the used pansharpening method.

The used pansharpening method includes three main parts: (1) spectral band combination, (2) spatial structure information extraction, and (3) spatial information injection. Initially, the intensity component is calculated by a linear combination of the spectral bands of the upsampled multispectral image. The high-frequency spatial details that only exist in the panchromatic image are then extracted by subtracting the intensity component from the histogram-matched PAN image. Finally, the extracted spatial structure information is injected into the multispectral image by the band-dependent injection weight.

3.5. Mosaicking

The images are registered in the pre-processing step; thus, registration is not conducted here. The radiometric differences of the neighbouring images should be reduced to make the mosaicked images as similar as possible visually. Radiometric normalization is selectively implemented because additional subtle radiometric adjustments will be implemented later. Seam line detection is helpful to obtain a boundary line where small radiation differences between the images are to be mosaicked. Around the seam line, image blending is operated, which aims to achieve a uniform transition on both sides of the seam line. However, in this section, emphasis is put on image blending, as the seam line detection can be automatically conducted in ENVI, or the image edge can be utilized as a seam line.

The radius for the image blending is then set on the basis of the overlapped area of the neighboring images. For image blending, as shown in Figure 8, the following equation is used to obtain the natural mosaicked images:

$$M(i,j) = \begin{cases} f_l(i,j) & (i,j) \in f_l \\ \omega_l(i,j) \times f_l(i,j) + \omega_r(i,j) \times f_r(i,j) & (i,j) \in (f_l \cap f_r) \\ f_r(i,j) & (i,j) \in f_r \end{cases} \quad (8)$$

where M is the mosaicked image and f_l and f_r are the left and right images to be mosaicked, respectively. ω_l and ω_r are the weights of the left and right images, respectively. (i,j) is the coordinate of the mosaicked image. Furthermore, if we set the feathering distance as q, then the weight can be calculated as follows:

$$\omega_r(i,j) = \frac{\sqrt{(i-i_l)^2 + (j-j_l)^2}}{q} \quad (9)$$

$$\omega_l(i,j) = 1 - \omega_r(i,j),\ i_l \le i \le i_r, j_l \le j \le j_r \quad (10)$$

where (i_l, j_l) and (i_r, j_r) are the coordinates of the left and right feathering edges. In this way, the grey value in the feathering distance gradually transitions from the left to the right image, thereby eliminating the seam line.

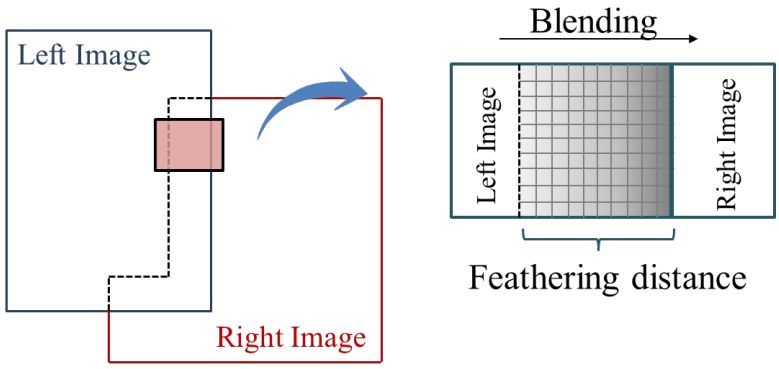

Figure 8. Illustration of image blending of left–right relation.

3.6. Post-Processing

In the post-processing steps, the main city area is clipped from the mosaicked image. In addition, the image is linearly stretched to ensure that the clipped urban image has good visual effects and to trim extreme values from both ends of the histogram using a specified percentage. Thus, the image contrast is improved for the final high-quality seamless urban image generation.

4. Experiments and Results

Section 4.1 presents a case application of urban map generation with the introduction to the experimental images and the final and intermediate results. Comparative experiments are conducted in Section 4.2 to evaluate the performance of the proposed thin and thick cloud removal methods.

4.1. Urban Map Generation Experiments and Results

The experimental images consisted of two types of Chinese high-resolution satellite images, namely Beijing-2 and Gaofen-2. The Beijing-2 images are delivered by the commercial TripleSat constellation, which is composed of three high-resolution satellites launched in 2014. Beijing-2 offers 1-m panchromatic and 4-m multispectral ground sampling distance imagery with a swath width of 23 km. Gaofen-2 is one of a series of high-resolution optical Earth observation satellites launched by the China National Space Administration. Moreover, Gaofen-2 is configured with two identical cameras and has been operational since October 2015. The two cameras on Gaofen-2 are capable of collecting images with 0.81-m panchromatic and 3.24-m multispectral bands, on a combined swath width of 45 km. The multispectral images of Beijing-2 and Gaofen-2 share a similar spectral band setting and spatial resolution, and both have three visible channels and a near-infrared channel. The Beijing-2 and Gaofen-2 images have been extensively used to provide Earth observation information for applications, such as monitoring land and water resources, agriculture, urban development, and environmental impact assessment.

The experimental images covered the main city areas of Nanning in Guangxi Zhuang Autonomous Region, China. Nanning is the capital city and the largest city of the Guangxi region, which is located in the southwest of China. All available images were classified into two categories, namely, the target images used to generate the final urban image of Nanning City and the auxiliary images used to remove cloud in the target images.

Table 1 shows the selected experimental images, in which the location, date and cloud cover percentages are provided, and the target and auxiliary images are numbered as T1–T5 and A1–A2, respectively. Specifically, the five Beijing-2 images acquired in October and December 2017 were considered as the target images to composite the main urban area of Nanning. Moreover, a Beijing-2 image acquired in May 2017 and a Gaofen-2 image acquired in October 2016 were used as the auxiliary images. All experimental images were level-1 data, that is, raw digital products with the process of homogenized radiation calibration. Figure 9 shows the distribution of the target images, in which the five Beijing-2 images cover the entire main city area of Nanning, and the yellow

boundary is the G7201 Nanning Ring Expressway. The adjacent images are mismatched at the borders and have evident radiometric inconsistencies. All four images are contaminated by haze and cloud, to different degrees.

Table 1. Experimental images for urban map generation of Nanning City.

Image Type	No.	Image ID	Centre Location	Date	Cloud Coverage *
Target	T1	TRIPLESAT_2_PMS_0010DDVI_007	E108.3_N22.8	9 October 2017	4.8%
	T2	TRIPLESAT_2_PMS_0010DDVI_008	E108.2_N33.0	9 October 2017	0.3%
	T3	TRIPLESAT_3_PMS_001397VI_006	E108.5_N22.7	2 December 2017	0.1%
	T4	TRIPLESAT_3_PMS_001397VI_007	E108.5_N22.9	2 December 2017	0.3%
	T5	TRIPLESAT_3_PMS_0013D6VI_007	E108.3_N22.7	17 December 2017	Clear
Auxiliary	A1	TRIPLESAT_1_PMS_000F58VI_002	E108.5_N22.9	27 May 2017	Clear
	A2	GF2_PMS1_0001881842	E108.3_N22.8	11 October 2016	1.0%

* The actual percentages of cloud cover are slightly higher than the given percentages, which were derived from the image header files.

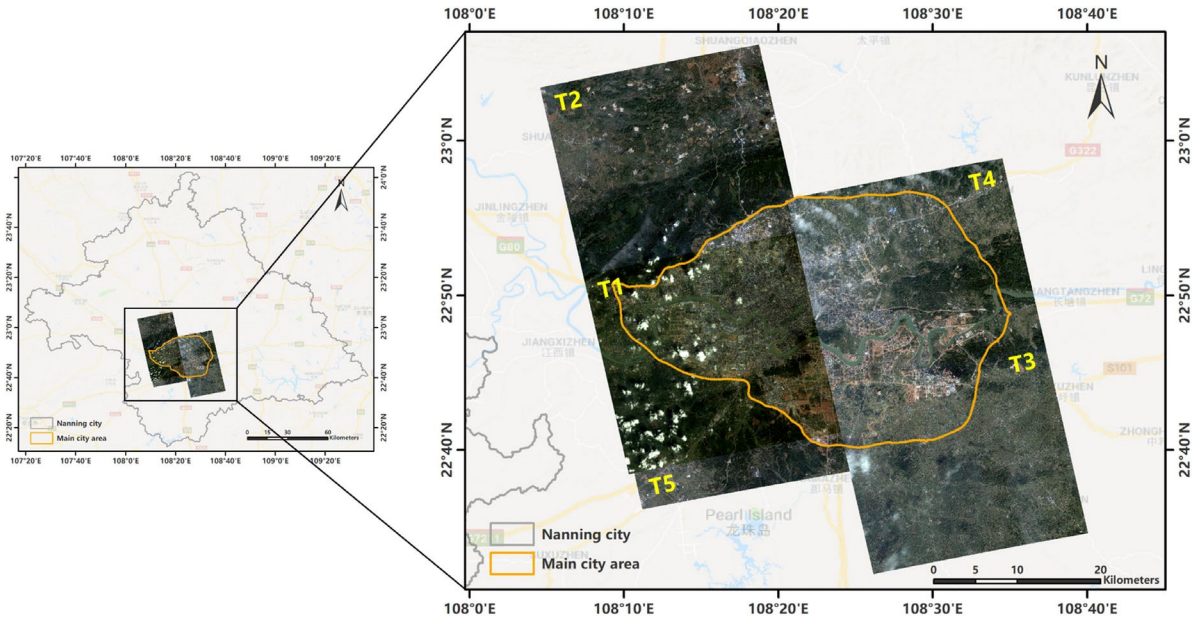

Figure 9. Study area and the distributions of the target experimental images.

Following the above procedure, a 0.91-m high-quality seamless main urban image of Nanning city was obtained. Generating this image took approximately 18 hours, which was implemented on a computer with an Intel Core i7-8700K 3.70 GHz CPU in the Windows 10 environment with 32 GB RAM. Notably, the necessary manual processing, which benefits the accuracy improvement and mainly includes manual interaction and mask correction, takes approximately 10% of the total processing time. In this subsection, the final experimental and intermediate results are shown to demonstrate the effectiveness and necessity of each step in the proposed procedure. Figure 10 shows

the generated urban image of Nanning City. The urban image generated by the proposed procedure is of high quality (cloud-free and clear), seamless (spatially continuous), and of high resolution (0.91-m resolution). In detail, no clouds can be found, and even by a careful check of the entire urban image, the buildings and roads are clear, as well as the open spaces, including the park, sports field and leisure square. The seam lines are eliminated well and cannot be visually identified. Thus, the generated image is spatially seamless. The pansharpened image has a high spatial resolution and keeps the abundant spectral information. The color of the water body of the Yongjiang River, which flows across the main city area of Nanning, is uniform.

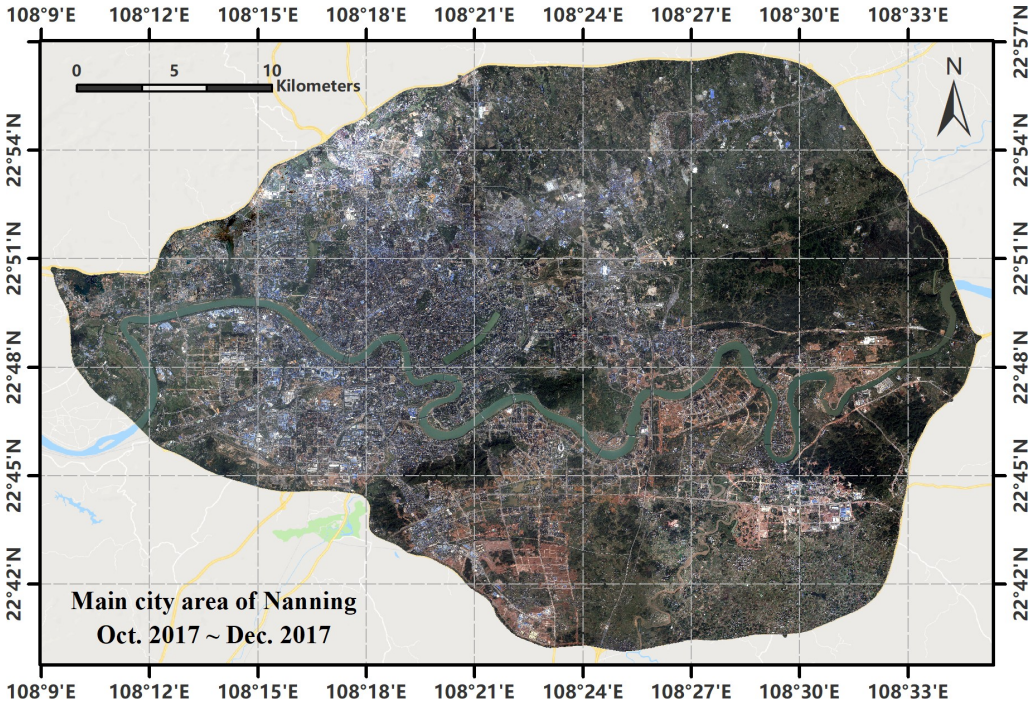

Figure 10. Generated a large-scale high-quality seamless urban image of Nanning City.

Examples are given by comparing the results before and after the specific processing, in terms of dehazing and thin cloud removal, thick cloud and shadow removal, image pansharpening and image mosaicking. The objective is to illustrate the local details of the generated image.

Haze and thin clouds are common in optical satellite images and result in information being partially missing in the image. A method of dehazing and thin cloud removal is utilized to recover the information in haze-covered areas. Figure 11 shows that the hazy images are enhanced, and the haze distributed over the urban and vegetated areas is removed. Moreover, the haze-free areas are unaffected and the details are well kept. However, the haze removal method cannot handle thick clouds and may cause residual cloud. Thus, thick cloud removal is subsequently undertaken.

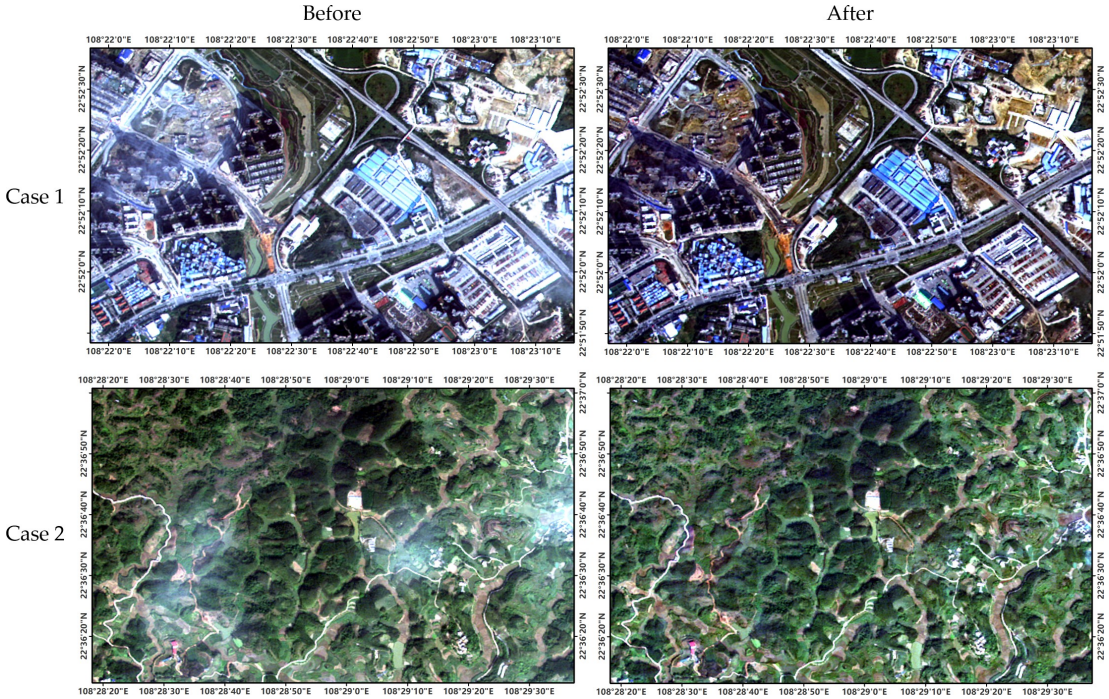

Figure 11. Examples of dehazing and thin cloud removal.

Differing from haze or thin clouds, thick clouds or shadows in images usually lead to information that is totally missing. In this case, we reconstruct the missing areas in the cloud-contaminated images with the aid of the auxiliary images of the same area, and thick cloud detection and cloud removal are utilized for reconstruction. Figure 12 displays the examples of cloud and shadow removal, in which cloud-contaminated images distributed over urban and vegetated areas are used. The cloud-removed images seem natural and have good color consistencies. In addition, the spatial details of the missing areas are well recovered, even where the missing areas are large, which indicates the effectiveness of the proposed cloud and shadow removal method.

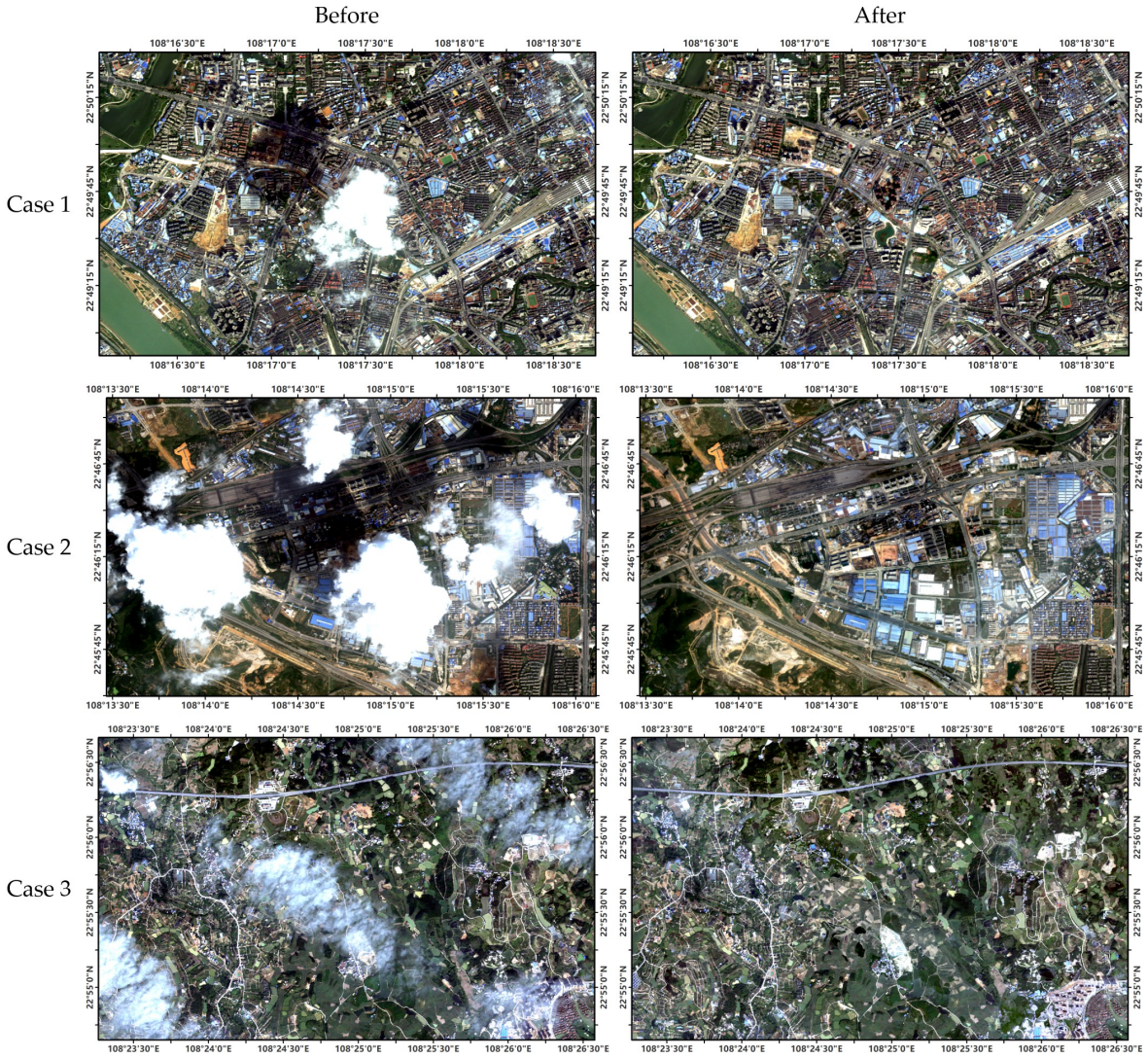

Figure 12. Examples of thick cloud and shadow removal.

Image pansharpening is essential for spatial resolution improvement, and it involves fusing the abundant spectral information in the multispectral image and the spatial details in the panchromatic image. Figure 13 shows the examples of the image pansharpening undertaken in this study, which show evident spatial detail improvements. In the first example, the cars on the bridge can be seen, and the outlines of the ships on the river are clear after pansharpening. The second and third examples are of a train station and circular interchange, respectively, in which the spatial details are clearly enhanced. The last example is a vegetated area, in which the colors of the trees and water are well kept from the original multispectral images. These examples demonstrate that the pansharpening method is an effective way to improve the spatial resolution of multispectral images.

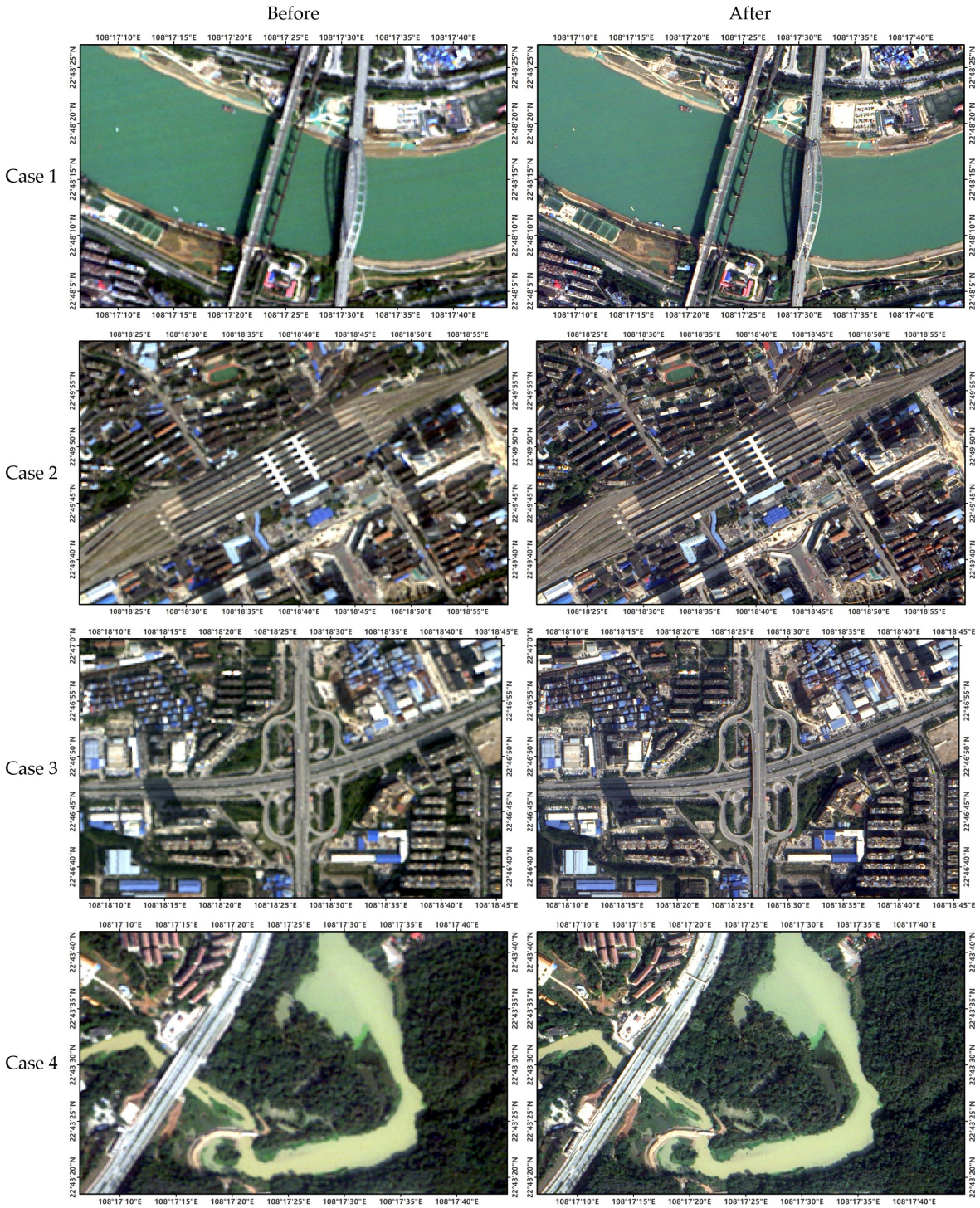

Figure 13. Examples of fast image pansharpening.

Mosaicking the neighboring images is a key step for the generation of the final urban image. In our implementation, the overlapping areas of the neighboring images are first registered. The order of mosaicking the images is then determined by the image date and the percentage of valid coverage, which means that an image which is closer to the target date and has a high coverage percentage of the target area has a higher priority. Finally, the images are mosaicked as described in Section 3.5. Figure 14 shows examples of image mosaicking in complex urban areas and a vegetated area. The misalignments between neighboring images are obvious, as well as the color differences, while the mosaicked images are seamless (spatially continuous) and have good color consistency. The results confirm that the applied image registration and mosaicking methods are effective.

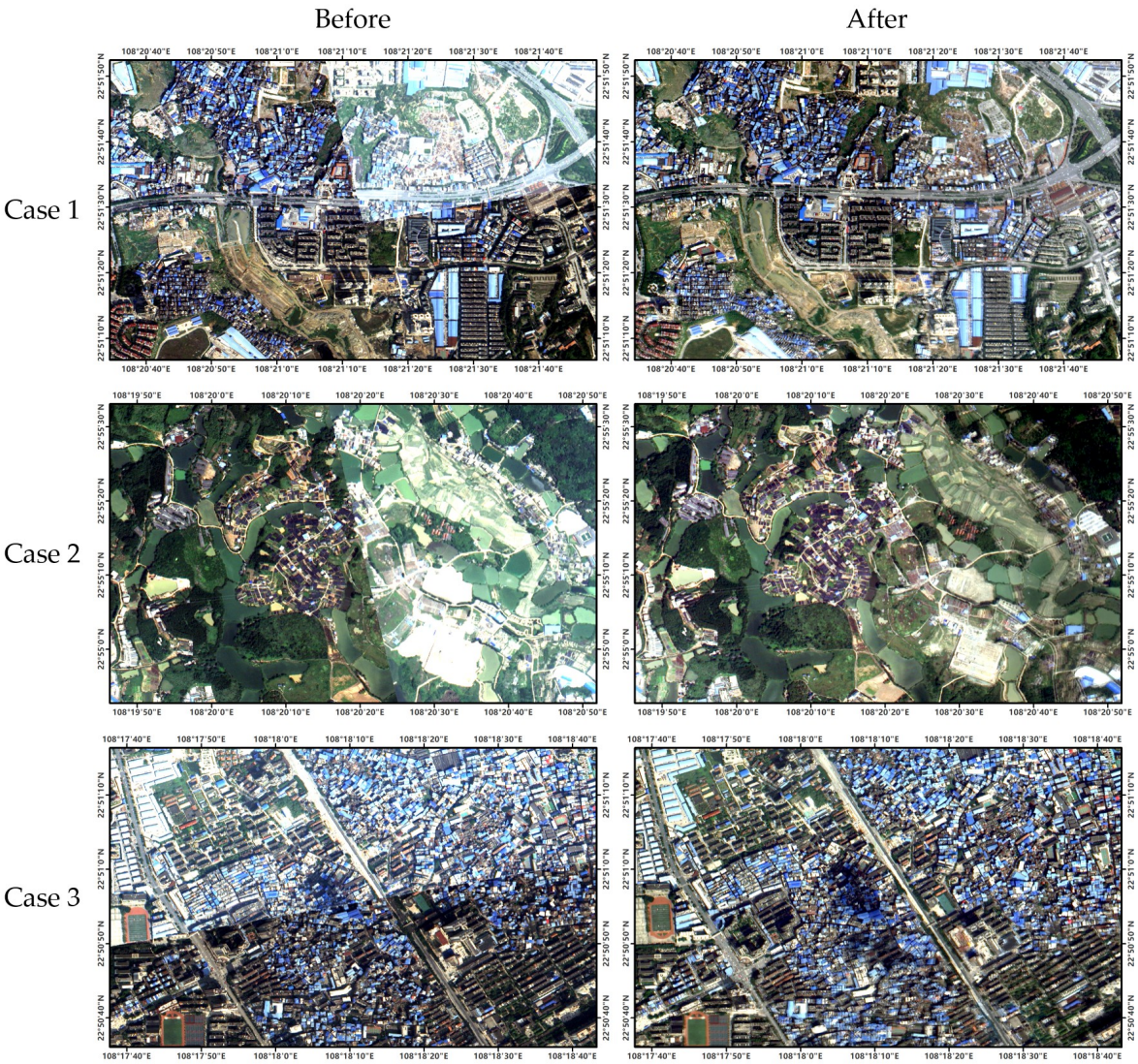

Figure 14. Examples of image mosaicking.

4.2. Comparative Experiments and Results

4.2.1. Comparisons of Dehazing and Thin Cloud Removal Methods

To validate the effectiveness of the haze removal method, two existing methods were selected for comparison, including the classical DCP method (CDCP) [21] and the dark channel-saturation prior method (DCSP) [84]. For a fair comparison, all parameters in these methods were set to be optimal via iterative adjustment.

Figure 15 shows the haze removal result for an urban area using different methods. Clearly, most of the image is covered by haze, making the brightness of the ground features higher than the actual values. The haze effects were largely eliminated, but certain residual haze can still be seen in the top left corner as indicated by the CDCP's result. Compared with CDCP, the haze removal capability of DCSP was weaker and the haze was still significant in the result. Figure 15d depicts the result of the proposed method. The high brightness caused by haze is completely eliminated, and the ground details were recovered well. Thus, the proposed method shows better performance than the comparison methods in removing haze for urban regions.

Figure 16 shows a haze removal instance for a forest area. The haze in the image was scattered and the intensity varies in spatial. Similar to Figure 15, CDCP removes the light haze but the dense one still remains. By contrast, DCSP's result is worse, where the haze cannot be removed but the

spectral of clear regions altered. The result of the proposed method indicates that the uneven haze contamination completely vanished, whereas the spectral of clear regions remains. The reason is that the proposed method fully considers the scattering variation spatially, and the non-uniform atmospheric model accurately describes the change. In summary, the proposed method holds superior capability in removing uneven haze and maintaining the spectral of clear regions, and benefits for generating high-quality and high-resolution seamless satellite imagery for large-scale urban regions.

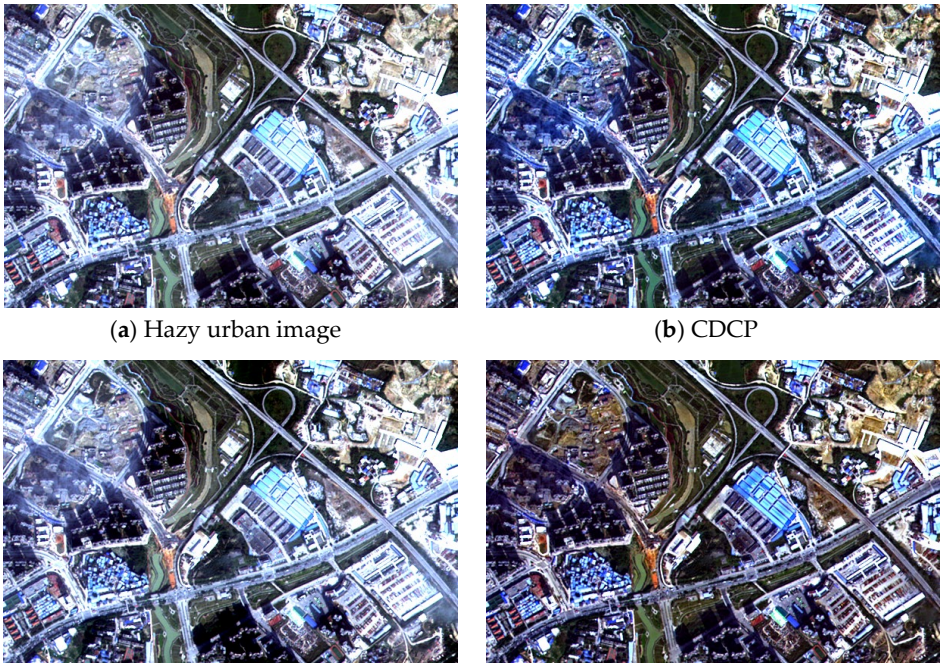

(**a**) Hazy urban image (**b**) CDCP

(**c**) DCSP (**d**) Proposed

Figure 15. Haze removal for an urban area using different methods. (**a**) Hazy urban image. (**c**–**d**) are haze removal results of CDCP, DCSP and the proposed method, respectively.

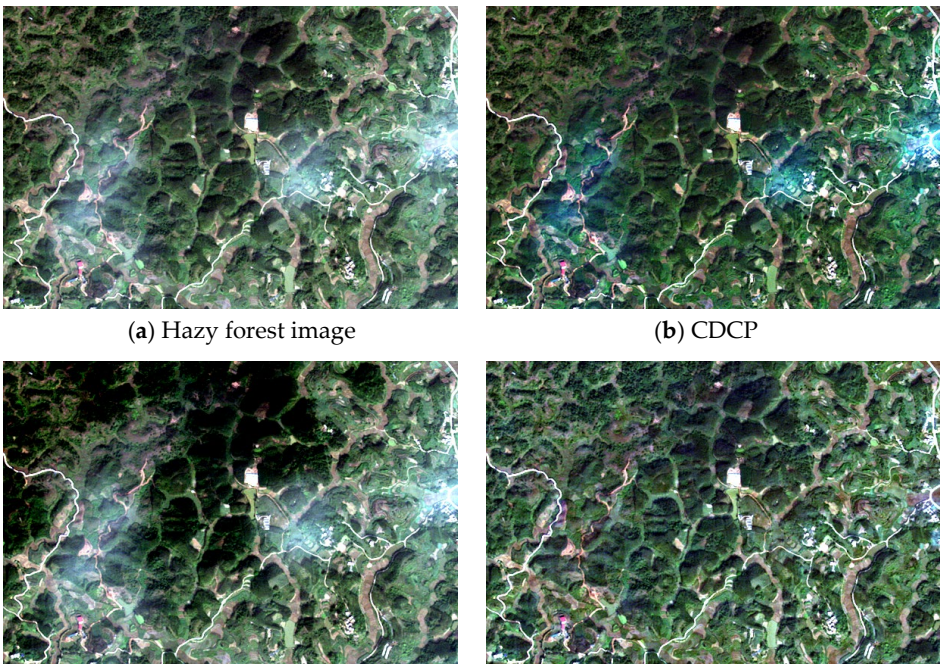

(**a**) Hazy forest image (**b**) CDCP

(**c**) DCSP (**d**) Proposed

Figure 16. Haze removal for a forest area using different methods. (**a**) Hazy forest image. (**c**–**d**) are haze removal results of CDCP, DCSP and the proposed method, respectively.

4.2.2. Comparisons Thick Cloud Removal Methods

In order to quantitatively evaluate the performance of the proposed SLMM method in cloud removal for high-resolution images, we simulated cloud-contaminated images by adding thick clouds to cloud-free Beijing-2 images used in this study, and measured the differences between the cloud removal results of SLMM and ground truths (i.e., original cloud-free images). Thick cloud removal methods, including localized linear histogram match (LLHM) [85] and modified neighborhood similar pixel interpolator (MNSPI) [86], are used for method comparisons. Correlation coefficient (CC), root-mean-square error (RMSE), universal image quality index (UIQI), and structural similarity (SSIM) index are utilized as the quantitative metrics for the accuracy evaluation of different methods.

We conduct two groups of simulated experiments, in which simulated thick clouds are added to vegetation and urban areas. Figure 17 shows the cloud removal results, and Table 2 lists their quantitative evaluation results. Accuracies are calculated only on the basis of the cloud removed areas and are the averaged values of four multispectral bands in Beijing-2 images. It can be seen that the proposed SLMM method achieves the best visual as well as quantitative results amongst the compared methods. Specifically, color distortion exists in the cloud removal results of LLHM (regions marked in red in Figure 17). By contrast, the results of MNSPI are influenced by the produced noises and artefacts, which lead to the loss of spatial details (regions marked in yellow in Figure 17). Thus, LLHM and MNSPI achieve lower CC and SSIM than SLMM. The cloud removal results of SLMM well preserve the spatial details and appear visually seamless in the recovered areas. Benefiting from the efficient implementation, SLMM is more effective than the other methods and takes 1.95 seconds to recover the two cloud-contaminated images in Figure 17 in total. By contrast, LLHM and MNSPI take 11.20 seconds and 166.31 seconds to accomplish the same tasks, respectively.

Although SLMM acquired the best cloud removal result, notably, the recovered spatial details in cloud removal results of SLMM are linearly transformed from the auxiliary image. Thus, the recovery accuracy will be influenced by the land cover changes between the cloud-contaminated and auxiliary images. Considering that SLMM is used to support the generation of yearly/seasonally urban geographical maps, the errors bringing from land cover changes between multitemporal images can be accepted to a certain degree.

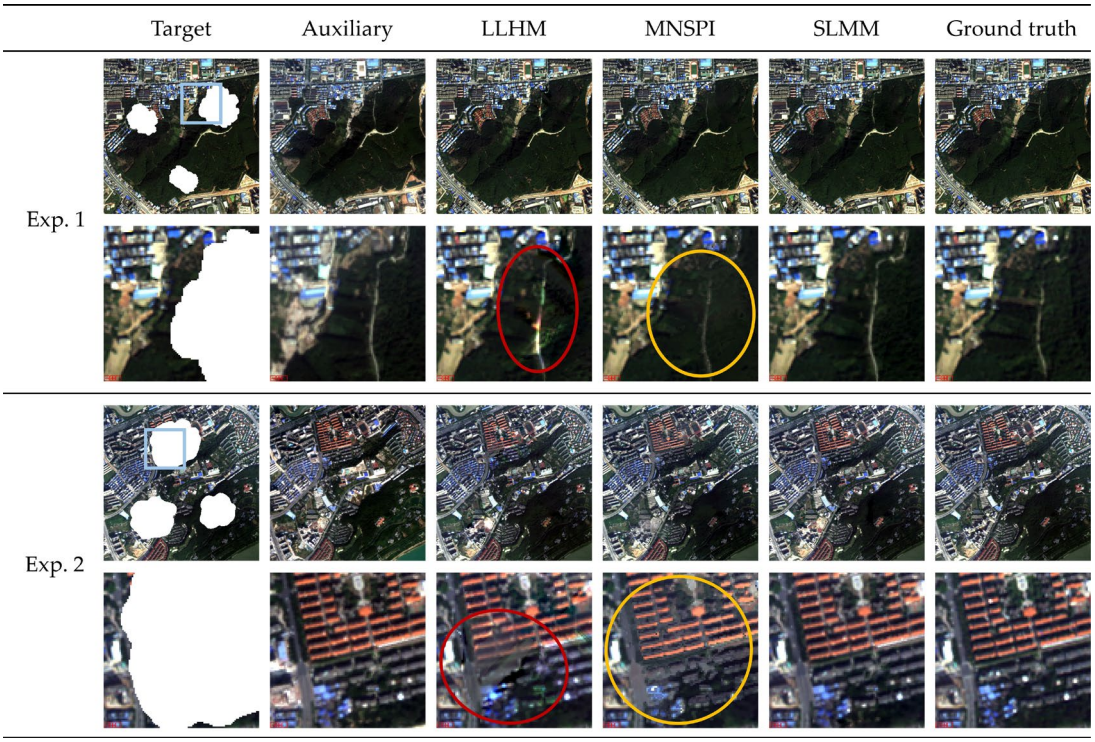

Figure 17. Simulated cloud removal experiment results of different methods.

Table 2. Quantitative evaluation results for the simulated cloud removal experiments.

	Method	CC (↑)	RMSE (↓)	UIQI (↑)	SSIM (↑)
Exp.1 in Figure 17	LLHM	0.747	0.045	0.735	0.820
	MNSPI	0.816	0.032	0.809	0.823
	SLMM	0.835	0.031	0.833	0.850
Exp.2 in Figure 17	LLHM	0.818	0.026	0.814	0.863
	MNSPI	0.860	0.020	0.847	0.879
	SLMM	0.886	0.019	0.886	0.890

5. Discussion

In the proposed procedure, a series of steps are utilized to achieve improvements in image quality and spatial resolution. However, errors are inevitable in each step; thus, the error sources and their influences were analyzed. The limitations of the applied methods were also discussed.

Image registration is a fundamental step that is aimed at eliminating the geometric misalignment and is of critical importance for multi-temporal thick cloud and shadow removal, as well as image mosaicking. Minor misalignment may remain between local regions of two temporal images, which may result in a slight spatial discontinuity in the boundaries of the cloud-removed areas and the seams of the images to be mosaicked.

In terms of dehazing and thin cloud removal, we only conduct this step on the hazy images. As the haze removal method is based on the concept of dark pixel, the approach will be efficient when the dark pixel exists and is sufficient in the study regions. However, when the dark pixel is lacking, for example, the bright soils, the method will be invalid and may cause color distortion (see Figure 18). Moreover, the method estimates the haze intensity with a slide overlapping window, assuming that the haze is uniform in local regions. Thus, for the haze contamination which varies violently in spatial, the over- or underestimated intensity will decrease the accuracy of the method, in which radiometric difference may occur in bright surface covered areas, but the radiometric normalization in the mosaicking reduces this kind of difference.

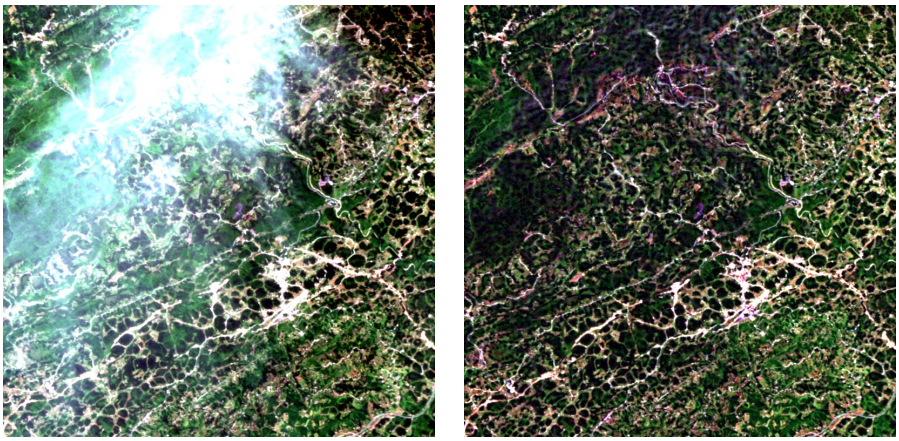

(**a**) (**b**)

Figure 18. Haze removal result with poor performance. (**a**) Hazy image. (**b**) Haze-removed image.

For thick-cloud detection and removal, manually corrections of cloud and clouds shadow masks are necessary in certain cases to ensure the complete recovery of contaminated areas. We instead use the similar pixel regression-based method of SLMM to preserve spatial details in the cloud-removed image, which are transformed from the auxiliary image, without changing the land-cover types. In this case, the abrupt temporal changes of land cover between the areas of the target cloudy image and auxiliary image may lead to spatial discontinuity around the boundaries of the cloud-removed areas.

The pansharpening method used in this study is effective and suitable for fast fusion large-scale remote sensing images. However, local spectral distortion may occur in large-scale image fusion, as shown in Figure 19a,b. Evident spectral inconsistencies exist between the observed LR-MS image (Figure 19a) and the fused HR-MS image (Figure 19b). Such inconsistencies may be due to the difference between the overall brightness and the local brightness of large-scale images and can be solved by residual correction. However, Figure 19a,b show that, in most cases, the local area with spectral distortion seems natural and consistent with human visual perception. Thus, no strategy has been applied. Furthermore, as an intermediate step in the entire process, the accuracy of pansharpening can be affected by the previous steps. Figure 19c,d present an example of low fusion accuracy. Figure 19c exhibits the blurry fusion result caused by low registration accuracy, and Figure 19d shows a clear fusion result after improving the registration accuracy.

Given that the experimental images may be different in other applications, the above errors are dependent on the actual cases of used images and applied methods. Our experience suggests that simple but effective methods are important for the processing of large-area and high-resolution satellite images.

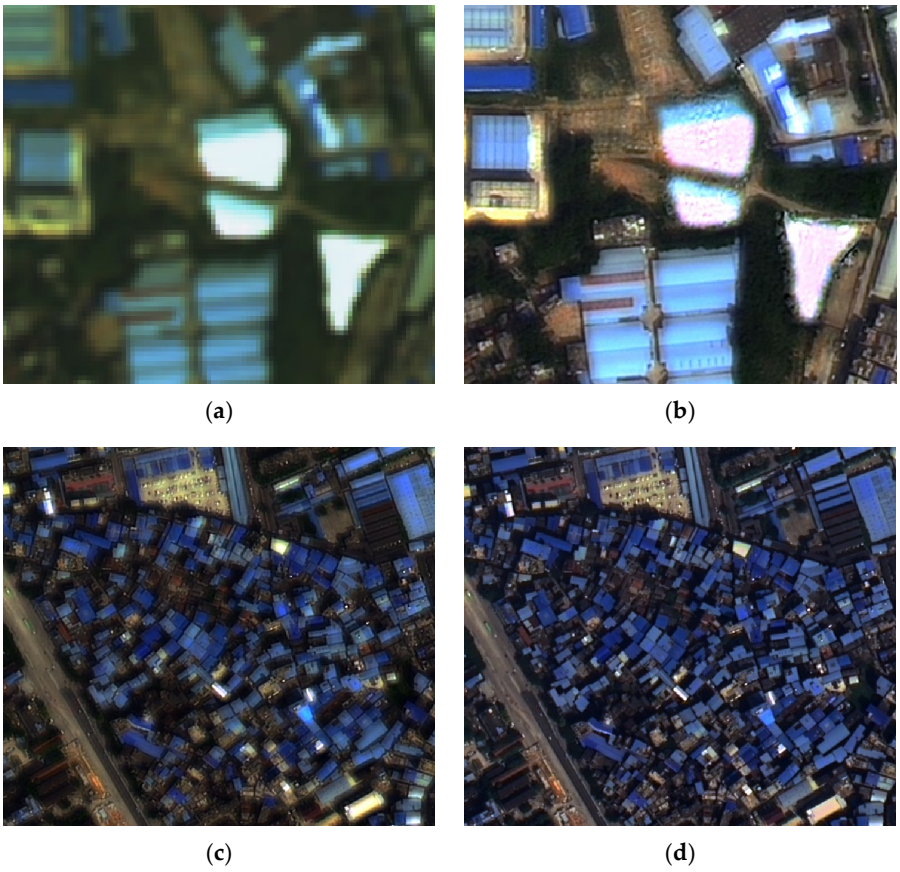

Figure 19. Fusion results with poor performance. (**a**) Observed LR-MS image. (**b**) Fused HR-MS image. (**c**) Blurry fusion result. (**d**) Clear fusion result.

6. Conclusions

Degradation factors, including haze, cloud, and cloud shadow, reduce the quality of optical remote sensing images, as well as the issues of geometric misalignment and radiometric inconsistency, making the generation of large-scale high-quality and seamless urban imagery a challenging task. In this study, a robust procedure for generating high-quality and seamless urban imagery is proposed. Specifically, a spatially adaptive method considering the uneven atmospheric scattering and a new algorithm (SLMM) are proposed to remove thin and thick clouds, respectively, and their effectiveness is verified by comparative experiments. A case application in Nanning City,

China, showed that the proposed procedure and methods are effective and can handle the complex issues of geometric misalignment, haze and cloud cover, pansharpening, and radiometric inconsistency. In our future study, additional effective methods in the presented procedure will be investigated to improve the generated urban image. Quality bands for the generated image, which track the processing errors in each step and mark the pixel quality, will also be constructed.

Author Contributions: The research topic was designed by X.L., Z.L. and H.S.; X.L., Z.L., R.F., S.L. and H.S. provided suggestions with regard to the method and experiments. X.L. and Z.L. performed the research and wrote the manuscript. Z.L., R.F., S.L., C.Z. and M.J. checked the experimental data, examined the experimental results, and participated in the revision of the manuscript. All authors have read and agreed to the published version of the manuscript.

Funding: This work was supported by the National Natural Science Foundation of China (NSFC) under grant nos. 41701394 and 41901357, the National Key R&D Program of China under grant nos. 2018YFA0605503 and 2017YFA0604402, the LIESMARS Special Research Funding, the Open Research Fund Program of the Key Laboratory of Digital Mapping and Land Information Application Engineering, Ministry of Natural Resources, under grant no. ZRZYBWD201903.

Acknowledgments: The authors would like to thank Wushuang Zhao, Yuanzheng Pi and Xiaoshuang Zhang for their efforts in pre-processing the experimental images.

Conflicts of Interest: The authors declare no conflict of interest.

References

1. Martinuzzi, S.; Gould, W.A.; Ramos González, O.M. Land development, land use, and urban sprawl in Puerto Rico integrating remote sensing and population census data. *Landsc. Urban Plan.* **2007**, *79*, 288–297, doi:10.1016/j.landurbplan.2006.02.014.
2. Xiao, J.; Shen, Y.; Ge, J.; Tateishi, R.; Tang, C.; Liang, Y.; Huang, Z. Evaluating urban expansion and land use change in Shijiazhuang, China, by using GIS and remote sensing. *Landsc. Urban Plan.* **2006**, *75*, 69–80, doi:10.1016/j.landurbplan.2004.12.005.
3. Hadeel, A.S.; Jabbar, M.T.; Chen, X. Application of remote sensing and GIS to the study of land use/cover change and urbanization expansion in Basrah province, southern Iraq. *Geo-Spat. Inf. Sci.* **2009**, *12*, 135–141, doi:10.1007/s11806-009-0244-7.
4. Piyoosh, A.K.; Ghosh, S.K. Semi-automatic mapping of anthropogenic impervious surfaces in an urban/suburban area using Landsat 8 satellite data. *GISci. Remote Sens.* **2017**, *54*, 471–494, doi:10.1080/15481603.2017.1282414.
5. Li, X.; Wang, L.; Cheng, Q.; Wu, P.; Gan, W.; Fang, L. Cloud removal in remote sensing images using nonnegative matrix factorization and error correction. *ISPRS J. Photogramm. Remote Sens.* **2019**, *148*, 103–113, doi:10.1016/j.isprsjprs.2018.12.013.
6. Li, X.; Shen, H.; Li, H.; Zhang, L. Patch matching-based multitemporal group sparse representation for the missing information reconstruction of remote-sensing images. *IEEE J. Sel. Top. Appl. Earth Obs. Remote Sens.* **2016**, *9*, 3629–3641, doi:10.1109/jstars.2016.2533547.
7. Shen, H.; Li, X.; Cheng, Q.; Zeng, C.; Yang, G.; Li, H.; Zhang, L. Missing information reconstruction of remote sensing data: A technical review. *IEEE Geosci. Remote Sens. Mag.* **2015**, *3*, 61–85, doi:10.1109/mgrs.2015.2441912.
8. Shen, H.; Meng, X.; Zhang, L. An integrated framework for the spatio-temporal-spectral fusion of remote sensing images. *IEEE Trans. Geosci. Remote Sens.* **2016**, *54*, 7135–7148, doi:10.1109/tgrs.2016.2596290.
9. Wei, Y.; Yuan, Q.; Shen, H.; Zhang, L. Boosting the accuracy of multispectral image pansharpening by learning a deep residual network. *IEEE Geosci. Remote Sens. Lett.* **2017**, *14*, 1795–1799, doi:10.1109/lgrs.2017.2736020.
10. Vivone, G.; Alparone, L.; Chanussot, J.; Mura, M.D.; Garzelli, A.; Licciardi, G.A.; Restaino, R.; Wald, L. A critical comparison among pansharpening algorithms. *IEEE Trans. Geosci. Remote Sens.* **2015**, *53*, 2565–2586, doi:10.1109/tgrs.2014.2361734.
11. Turner, P.J.; Prata, A.J.; Howden, R.T.; Houghton, N.R.; Taylor, A. An ATSR-2 mosaic image of Australia. *Int. J. Remote Sens.* **2001**, *22*, 3889–3894, doi:10.1080/01431160110069872.
12. Helmer, E.H.; Ruefenacht, B. Cloud-free satellite image mosaics with regression trees and histogram

matching. *Photogramm. Eng. Remote Sens.* **2005**, *71*, 1079–1089, doi:10.14358/pers.71.9.1079.
13. Haas, J.; Ban, Y. Urban growth and environmental impacts in Jing-Jin-Ji, the Yangtze, River Delta and the Pearl River Delta. *Int. J. Appl. Earth Obs. Geoinf.* **2014**, *30*, 42–55, doi:10.1016/j.jag.2013.12.012.
14. Li, X.; Hui, N.; Shen, H.; Fu, Y.; Zhang, L. A robust mosaicking procedure for high spatial resolution remote sensing images. *ISPRS J. Photogramm. Remote Sens.* **2015**, *109*, 108–125, doi:10.1016/j.isprsjprs.2015.09.009.
15. Chon, J.; Kim, H.; Lin, C.-S. Seam-line determination for image mosaicking: A technique minimizing the maximum local mismatch and the global cost. *ISPRS J. Photogramm. Remote Sens.* **2010**, *65*, 86–92, doi:10.1016/j.isprsjprs.2009.09.001.
16. Wang, M.; Yuan, S.; Pan, J.; Fang, L.; Zhou, Q.; Yang, G. Seamline determination for high resolution orthoimage mosaicking using watershed segmentation. *Photogramm. Eng. Remote Sens.* **2016**, *82*, 121–133, doi:10.14358/pers.82.2.121.
17. Shen, H.; Li, H.; Qian, Y.; Zhang, L.; Yuan, Q. An effective thin cloud removal procedure for visible remote sensing images. *ISPRS J. Photogramm. Remote Sens.* **2014**, *96*, 224–235, doi:10.1016/j.isprsjprs.2014.06.011.
18. Liang, S.; Fang, H.; Chen, M. Atmospheric correction of Landsat ETM+ land surface imagery. I. Methods. *IEEE Trans. Geosci. Remote Sens.* **2001**, *39*, 2490–2498, doi:10.1109/36.964986.
19. Richter, R.; Schläpfer, D. Geo-atmospheric processing of airborne imaging spectrometry data. Part 2: Atmospheric/topographic correction. *Int. J. Remote Sens.* **2002**, *23*, 2631–2649, doi:10.1080/01431160110115834.
20. Liu, J.; Wang, X.; Chen, M.; Liu, S.; Zhou, X.; Shao, Z.; Liu, P. Thin cloud removal from single satellite images. *Opt. Express* **2014**, *22*, 618–632, doi:10.1364/oe.22.000618.
21. He, K.; Sun, J.; Tang, X. Single image haze removal using dark channel prior. *IEEE Trans. Pattern Anal. Mach. Intell.* **2011**, *33*, 2341–2353, doi:10.1109/tpami.2010.168.
22. Liu, Q.; Gao, X.; He, L.; Lu, W. Haze removal for a single visible remote sensing image. *Signal Process.* **2017**, *137*, 33–43, doi:10.1016/j.sigpro.2017.01.036.
23. Makarau, A.; Richter, R.; Müller, R.; Reinartz, P. Haze detection and removal in remotely sensed multispectral imagery. *IEEE Trans. Geosci. Remote Sens.* **2014**, *52*, 5895–5905, doi:10.1109/tgrs.2013.2293662.
24. Makarau, A.; Richter, R.; Schläpfer, D.; Reinartz, P. Combined haze and cirrus removal for multispectral imagery. *IEEE Geosci. Remote Sens. Lett.* **2016**, *13*, 379–383, doi:10.1109/lgrs.2016.2515110.
25. Chen, S.; Chen, X.; Chen, J.; Jia, P.; Cao, X.; Liu, C. An iterative haze optimized transformation for automatic cloud/haze detection of Landsat imagery. *IEEE Trans. Geosci. Remote Sens.* **2016**, *54*, 2682–2694, doi:10.1109/tgrs.2015.2504369.
26. Chen, S.; Chen, X.; Chen, X.; Chen, J.; Cao, X.; Shen, M.; Yang, W.; Cui, X. A novel cloud removal method based on IHOT and the cloud trajectories for Landsat imagery. *Remote Sens.* **2018**, *10*, 1040, doi:10.3390/rs10071040.
27. Shen, Y.; Wang, Y.; Lv, H.; Qian, J. Removal of thin clouds in Landsat-8 OLI data with independent component analysis. *Remote Sens.* **2015**, *7*, 11481–11500, doi:10.3390/rs70911481.
28. Zhang, Y.; Guindon, B.; Cihlar, J. An image transform to characterize and compensate for spatial variations in thin cloud contamination of Landsat images. *Remote Sens. Environ.* **2002**, *82*, 173–187, doi:10.1016/S0034-4257(02)00034-2.
29. Lv, H.; Wang, Y.; Shen, Y. An empirical and radiative transfer model based algorithm to remove thin clouds in visible bands. *Remote Sens. Environ.* **2016**, *179*, 183–195, doi:10.1016/j.rse.2016.03.034.
30. Braaten, J.D.; Cohen, W.B.; Yang, Z. Automated cloud and cloud shadow identification in Landsat MSS imagery for temperate ecosystems. *Remote Sens. Environ.* **2015**, *169*, 128–138, doi:10.1016/j.rse.2015.08.006.
31. Zhai, H.; Zhang, H.; Zhang, L.; Li, P. Cloud/shadow detection based on spectral indices for multi/hyperspectral optical remote sensing imagery. *ISPRS J. Photogramm. Remote Sens.* **2018**, *144*, 235–253, doi:10.1016/j.isprsjprs.2018.07.006.
32. Zhu, Z.; Woodcock, C.E. Object-based cloud and cloud shadow detection in Landsat imagery. *Remote Sens. Environ.* **2012**, *118*, 83–94, doi:10.1016/j.rse.2011.10.028.
33. Li, Z.; Shen, H.; Li, H.; Xia, G.; Gamba, P.; Zhang, L. Multi-feature combined cloud and cloud shadow detection in GaoFen-1 wide field of view imagery. *Remote Sens. Environ.* **2017**, *191*, 342–358, doi:10.1016/j.rse.2017.01.026.
34. Bai, T.; Li, D.; Sun, K.; Chen, Y.; Li, W. Cloud detection for high-resolution satellite imagery using machine learning and multi-feature fusion. *Remote Sens.* **2016**, *8*, 715, doi:10.3390/rs8090715.
35. Li, Z.; Shen, H.; Cheng, Q.; Liu, Y.; You, S.; He, Z. Deep learning based cloud detection for medium and high resolution remote sensing images of different sensors. *ISPRS J. Photogramm. Remote Sens.* **2019**, *150*, 197–212, doi:10.1016/j.isprsjprs.2019.02.017.
36. Li, X.; Shen, H.; Zhang, L.; Zhang, H.; Yuan, Q.; Yang, G. Recovering quantitative remote sensing products

contaminated by thick clouds and shadows using multitemporal dictionary learning. *IEEE Trans. Geosci. Remote Sens.* **2014**, *52*, 7086–7098, doi:10.1109/tgrs.2014.2307354.

37. Chen, B.; Huang, B.; Chen, L.; Xu, B. Spatially and temporally weighted regression: A novel method to produce continuous cloud-free Landsat imagery. *IEEE Trans. Geosci. Remote Sens.* **2017**, *55*, 27–37, doi:10.1109/tgrs.2016.2580576.
38. Padhee, S.K.; Dutta, S. Spatio-temporal reconstruction of MODIS NDVI by regional land surface phenology and harmonic analysis of time-series. *GISci. Remote Sens.* **2019**, *56*, 1261–1288, doi:10.1080/15481603.2019.1646977.
39. Cheng, Q.; Shen, H.; Zhang, L.; Yuan, Q.; Zeng, C. Cloud removal for remotely sensed images by similar pixel replacement guided with a spatio-temporal MRF model. *ISPRS J. Photogramm. Remote Sens.* **2014**, *92*, 54–68, doi:10.1016/j.isprsjprs.2014.02.015.
40. Lin, C.; Tsai, P.; Lai, K.; Chen, J. Cloud removal from multitemporal satellite images using information cloning. *IEEE Trans. Geosci. Remote Sens.* **2013**, *51*, 232–241, doi:10.1109/tgrs.2012.2197682.
41. Li, Z.; Shen, H.; Cheng, Q.; Li, W.; Zhang, L. Thick cloud removal in high-resolution satellite images using stepwise radiometric adjustment and residual correction. *Remote Sens.* **2019**, *11*, 1925, doi:10.3390/rs11161925.
42. Aiazzi, B.; Baronti, S.; Selva, M. Improving component substitution pansharpening through multivariate regression of MS+Pan data. *IEEE Trans. Geosci. Remote Sens.* **2007**, *45*, 3230–3239, doi:10.1109/tgrs.2007.901007.
43. Xu, Q.; Li, B.; Zhang, Y.; Ding, L. High-fidelity component substitution pansharpening by the fitting of substitution data. *IEEE Trans. Geosci. Remote Sens.* **2014**, *52*, 7380–7392, doi:10.1109/tgrs.2014.2311815.
44. Meng, X.; Li, J.; Shen, H.; Zhang, L.; Zhang, H. Pansharpening with a guided filter based on three-layer decomposition. *Sensors* **2016**, *16*, 1068, doi:10.3390/s16071068.
45. Shahdoosti, H.R.; Javaheri, N. Pansharpening of Clustered MS and pan images considering mixed pixels. *IEEE Geosci. Remote Sens. Lett.* **2017**, *14*, 826–830, doi:10.1109/lgrs.2017.2682122.
46. Wald, L.; Ranchin, T. Liu 'Smoothing filter-based intensity modulation: A spectral preserve image fusion technique for improving spatial details'. *Int. J. Remote Sens.* **2002**, *23*, 593–597, doi:10.1080/01431160110088772.
47. Aiazzi, B.; Alparone, L.; Baronti, S.; Garzelli, A.; Selva, M. MTF-tailored multiscale fusion of high-resolution MS and pan imagery. *Photogramm. Eng. Remote Sens.* **2006**, *72*, 591–596, doi:10.14358/pers.72.5.591.
48. Zhang, L.; Shen, H.; Gong, W.; Zhang, H. Adjustable model-based fusion method for multispectral and panchromatic images. *IEEE Trans. Syst. Man Cybern. Part B (Cybern.)* **2012**, *42*, 1693–1704, doi:10.1109/tsmcb.2012.2198810.
49. Liu, P.; Xiao, L.; Zhang, J.; Naz, B. Spatial-Hessian-feature-guided variational model for pan-sharpening. *IEEE Trans. Geosci. Remote Sens.* **2016**, *54*, 2235–2253, doi:10.1109/tgrs.2015.2497966.
50. Jiang, C.; Zhang, H.; Shen, H.; Zhang, L. Two-step sparse coding for the pan-sharpening of remote sensing images. *IEEE J. Sel. Top. Appl. Earth Obs. Remote Sens.* **2014**, *7*, 1792–1805, doi:10.1109/jstars.2013.2283236.
51. Masi, G.; Cozzolino, D.; Verdoliva, L.; Scarpa, G. Pansharpening by convolutional neural networks. *Remote Sens.* **2016**, *8*, 594–615, doi:10.3390/rs8070594.
52. Yuan, Q.; Wei, Y.; Meng, X.; Shen, H.; Zhang, L. A Multiscale and multidepth convolutional neural network for remote sensing imagery pan-sharpening. *IEEE J. Sel. Top. Appl. Earth Obs. Remote Sens.* **2018**, *11*, 978–989, doi:10.1109/jstars.2018.2794888.
53. Brown, M.; Lowe, D.G. Automatic panoramic image stitching using invariant features. *Int. J. Comput. Vis.* **2007**, *74*, 59–73, doi:10.1007/s11263-006-0002-3.
54. Feng, R.; Du, Q.; Li, X.; Shen, H. Robust registration for remote sensing images by combining and localizing feature- and area-based methods. *ISPRS J. Photogramm. Remote Sens.* **2019**, *151*, 15–26, doi:10.1016/j.isprsjprs.2019.03.002.
55. Li, X.; Feng, R.; Guan, X.; Shen, H.; Zhang, L. Remote sensing image mosaicking: Achievements and challenges. *IEEE Geosci. Remote Sens. Mag.* **2019**, *7*, 8–22, doi:10.1109/MGRS.2019.2921780.
56. Wong, A.; Clausi, D.A. ARRSI: Automatic registration of remote-sensing images. *IEEE Trans. Geosci. Remote Sens.* **2007**, *45*, 1483–1493, doi:10.1109/tgrs.2007.892601.
57. Cole-Rhodes, A.A.; Johnson, K.L.; LeMoigne, J.; Zavorin, I. Multiresolution registration of remote sensing imagery by optimization of mutual information using a stochastic gradient. *IEEE Trans. Image Process.* **2003**, *12*, 1495–1511, doi:10.1109/tip.2003.819237.
58. Hel-Or, Y.; Hel-Or, H.; David, E. Fast template matching in non-linear tone-mapped images. In Proceedings of the International Conference on Computer Vision (ICCV), Barcelona, Spain, 6–13 November 2011; pp. 1355–1362.
59. Lowe, D.G. Distinctive image features from scale-invariant keypoints. *Int. J. Comput. Vis.* **2004**, *60*, 91–110, doi:10.1023/b:visi.0000029664.99615.94.

60. Bay, H.; Tuytelaars, T.; Van Gool, L. SURF: Speeded up robust features. In Proceedings of the Computer Vision—ECCV 2006 9th European Conference on Computer Vision, Graz, Austria, 7–13 May 2006; pp. 404–417.
61. Xie, R.; Xia, M.; Yao, J.; Li, L. Guided color consistency optimization for image mosaicking. *ISPRS J. Photogramm. Remote Sens.* **2018**, *135*, 43–59, doi:10.1016/j.isprsjprs.2017.11.012.
62. Yu, L.; Zhang, Y.; Sun, M.; Zhou, X.; Liu, C. An auto-adapting global-to-local color balancing method for optical imagery mosaic. *ISPRS J. Photogramm. Remote Sens.* **2017**, *132*, 1–19, doi:10.1016/j.isprsjprs.2017.08.002.
63. Oliveira, M.; Sappa, A.D.; Santos, V. A probabilistic approach for color correction in image mosaicking applications. *IEEE Trans. Image Process.* **2015**, *24*, 508–523, doi:10.1109/tip.2014.2375642.
64. Chen, C.; Chen, Z.; Li, M.; Liu, Y.; Cheng, L.; Ren, Y. Parallel relative radiometric normalisation for remote sensing image mosaics. *Comput. Geosci.* **2014**, *73*, 28–36, doi:10.1016/j.cageo.2014.08.007.
65. Storey, E.A.; Stow, D.A.; Plummer, M.J. Normalizing shadows in multi-temporal aerial frame imagery using relative radiometric adjustments to support near-real-time change detection. *GISci. Remote Sens.* **2019**, *56*, 22–42, doi:10.1080/15481603.2018.1489446.
66. Li, L.; Yao, J.; Lu, X.; Tu, J.; Shan, J. Optimal seamline detection for multiple image mosaicking via graph cuts. *ISPRS J. Photogramm. Remote Sens.* **2016**, *113*, 1–16, doi:10.1016/j.isprsjprs.2015.12.007.
67. Chen, G.; Chen, S.; Li, X.; Zhou, P.; Zhou, Z. Optimal seamline detection for orthoimage mosaicking based on DSM and improved JPS algorithm. *Remote Sens.* **2018**, *10*, 821, doi:10.3390/rs10060821.
68. Pan, J.; Zhou, Q.; Wang, M. Seamline determination based on segmentation for urban image mosaicking. *IEEE Geosci. Remote Sens. Lett.* **2014**, *11*, 1335–1339, doi:10.1109/lgrs.2013.2293197.
69. Nguyen, T.L.; Byun, Y.; Han, D.; Huh, J. Efficient seamline determination for UAV image mosaicking using edge detection. *Remote Sens. Lett.* **2018**, *9*, 763–769, doi:10.1080/2150704x.2018.1475772.
70. Du, Q.; Raksuntorn, N.; Orduyilmaz, A.; Bruce, L.M. Automatic registration and mosaicking for airborne multispectral image sequences. *Photogramm. Eng. Remote Sens.* **2008**, *74*, 169–181, doi:10.14358/pers.74.2.169.
71. Merson, R.H. An AVHRR mosaic image of Antarctica. *Int. J. Remote Sens.* **1989**, *10*, 669–674, doi:10.1080/01431168908903908.
72. Roy, D.P.; Ju, J.; Kline, K.; Scaramuzza, P.L.; Kovalskyy, V.; Hansen, M.; Loveland, T.R.; Vermote, E.; Zhang, C. Web-enabled Landsat data (WELD): Landsat ETM+ composited mosaics of the conterminous United States. *Remote Sens. Environ.* **2010**, *114*, 35–49, doi:10.1016/j.rse.2009.08.011.
73. Fraser, A.D.; Massom, R.A.; Michael, K.J. A method for compositing polar MODIS satellite images to remove cloud cover for Landfast sea-ice detection. *IEEE Trans. Geosci. Remote Sens.* **2009**, *47*, 3272–3282, doi:10.1109/tgrs.2009.2019726.
74. Fraser, A.D.; Massom, R.A.; Michael, K.J. Generation of high-resolution East Antarctic landfast sea-ice maps from cloud-free MODIS satellite composite imagery. *Remote Sens. Environ.* **2010**, *114*, 2888–2896, doi:10.1016/j.rse.2010.07.006.
75. Hewson, R.D.; Cudahy, T.J.; Mizuhiko, S.; Ueda, K.; Mauger, A.J. Seamless geological map generation using ASTER in the Broken Hill-Curnamona province of Australia. *Remote Sens. Environ.* **2005**, *99*, 159–172, doi:10.1016/j.rse.2005.04.025.
76. Zhang, Y.; Wan, Y.; Wang, B.; Kang, Y.; Xiong, J. Automatic processing of Chinese GF-1 wide field of view images. *Int. Arch. Photogramm. Remote Sens. Spat. Inf. Sci.* **2015**, *XL-7/W3*, 729–734, doi:10.5194/isprsarchives-XL-7-W3-729-2015.
77. Li, M.; Liew, S.C.; Kwoh, L.K. Producing cloud free and cloud-shadow free mosaic from cloudy IKONOS images. In Proceedings of the International Geoscience and Remote Sensing Symposium (IGARSS), Toulouse, France, 21–25 July 2003, doi:10.1109/IGARSS.2003.1295323.
78. Du, Y.; Cihlar, J.; Beaubien, J.; Latifovic, R. Radiometric normalization, compositing, and quality control for satellite high resolution image mosaics over large areas. *IEEE Trans. Geosci. Remote Sens.* **2001**, *39*, 623–634, doi:10.1109/36.911119.
79. Scheidt, S.; Ramsey, M.; Lancaster, N. Radiometric normalization and image mosaic generation of ASTER thermal infrared data: An application to extensive sand sheets and dune fields. *Remote Sens. Environ.* **2008**, *112*, 920–933, doi:10.1016/j.rse.2007.06.020.
80. Jiang, H.; Lu, N.; Yao, L.; Zhang, X. Single image dehazing for visible remote sensing based on tagged haze thickness maps. *Remote Sens. Lett.* **2018**, *9*, 627–635, doi:10.1080/2150704x.2018.1456701.
81. Narasimhan, S.G.; Nayar, S.K. Vision and the atmosphere. *Int. J. Comput. Vis.* **2002**, *48*, 233–254, doi:10.1023/a:1016328200723.

82. Narasimhan, S.G.; Nayar, S.K. Contrast restoration of weather degraded images. *IEEE Trans. Pattern Anal. Mach. Intell.* **2003**, *25*, 713–724.
83. Meng, X.; Shen, H.; Li, H.; Zhang, L.; Fu, R. Review of the pansharpening methods for remote sensing images based on the idea of meta-analysis: Practical discussion and challenges. *Inf. Fusion* **2019**, *46*, 102–113, doi:10.1016/j.inffus.2018.05.006.
84. Xie, F.Y.; Chen, J.J.; Pan, X.X.; Jiang, Z.G. Adaptive haze removal for single remote sensing image. *IEEE Access* **2018**, *6*, 67982–67991, doi:10.1109/Access.2018.2879893.
85. Scaramuzza, P.; Barsi, J. Landsat 7 scan line corrector-off gap-filled product development. In Proceedings of the Pecora 16 Conference on Global Priorities in Land Remote Sensing, Sioux Falls, SD, USA, 23–27 October 2005; pp. 23–27.
86. Zhu, X.; Gao, F.; Liu, D.; Chen, J. A modified neighborhood similar pixel interpolator approach for removing thick clouds in Landsat images. *IEEE Geosci. Remote Sens. Lett.* **2011**, *9*, 521–525.